Osaka University Knowledge Archive

Title	Electrical transport properties in phase-separated manganite studied by terahertz time domain spectroscopy
Author(s)	Nguyen, Thi Van Anh
Citation	大阪大学, 2015, 博士論文
Version Type	VoR
URL	https://doi.org/10.18910/53959
rights	
Note	

Osaka University Knowledge Archive : OUKA

https://ir.library.osaka-u.ac.jp/

Osaka University

Electrical transport properties in phase-separated manganite studied by terahertz time domain spectroscopy

NGUYEN THI VAN ANH

SEPTEMBER 2015

Electrical transport properties in phase-separated manganite studied by terahertz time domain spectroscopy

A dissertation submitted to

THE GRADUATE SCHOOL OF ENGINEERING SCIENCE
OSAKA UNIVERSITY

in partial fulfillment of the requirements for the degree of

DOCTOR OF PHILOSOPHY IN SCIENCE

BY

NGUYEN THI VAN ANH

SEPTEMBER 2015

Abstract

The transition metal oxides with strongly correlated electrons have emerged as exotic materials with various functionalities such as the colossal magnetoresistivity in manganites. Of particular interest is a typical perovskite manganite (La,Pr,Ca)MnO_3 (LPCMO) which exhibits the insulator - metal transition (IMT) originating from the coexistence of metal and insulator domains in a nanometer scale. Interestingly, peculiar functionalities can be expected in the nanometer scale mixed-phase materials in which the electronic domains were confined. To understand their nanopeculiar conductive property, the quantitative estimation of domain evolution which shows the temperature-induced fraction change of metallic domain ($X(T)$) in the coexistence phenomena becomes extremely important. Moreover, the estimation of dc conductivity ($\sigma_{dc}(T)$) for nanoscale electronic domains is also vital not only in elucidating the IMT behavior, but also in designing new functional oxide nano electronics devices.

In this thesis, I have successfully developed an efficient technique to investigate the transport dynamics in nanoscale phase-separated materials by taking advantage of terahertz time domain spectroscopy (THz-TDS). My achievements are listed in following parts:

(1) I established the technique to investigate electrical transport properties, i.e., the simultaneous evaluation of $X(T)$ and $\sigma_{dc}(T)$ in a LPCMO film by the THz-TDS. I obtained the THz conductivity behavior at different temperatures ($\sigma_{THz}(\omega,T)$ curves) for the film, and then I proposed an original "insulator-metal composited model" to successfully explain the change of $\sigma_{THz}(\omega,T)$ behavior through the IMT. This model enabled us to estimate the electrical transport properties for a mixed-phase oxide film in a non-contact manner. This technique is applicable for other mixed-phase nanostructured materials.

(2) I successfully estimated the electrical transport properties in a 100-nm-width LPCMO nanowires sample through the IMT using the THz-TDS. By aligning the high-density nanowires parallel to the polarization direction of THz pulse, I obtained their characteristic conductivity behavior $\sigma_{THz}(\omega,T)$. The $X(T)$, estimated by fitting $\sigma_{THz}(\omega,T)$ curves based on my proposed insulator-metal composite model, revealed the rapid change of electronic domain from metal to insulator with increasing temperature in comparison with the conventional film sample. Simultaneously this technique enabled us to evaluate the $\sigma_{dc}(T)$ for nanowires without attaching electrodes, indicating that this is a powerful tool for study the electrical transport properties in nanostructured materials.

(3) As a development of nanostructure fabrication, I successfully produced the manganite nanobox array structures with precise control their wall-width down to 30 nm using an original three-dimensional (3D) nanotemplate pulsed laser deposition technique (PLD). The X-ray photoemission spectroscopy on the manganite nanoboxes structure indicated their peculiar IMT functionality. The nano-oxides fabricated by this 3D nanotemplate PLD technique will be one of good candidates for future applications in nano-oxide-electronics.

CONTENTS

CHAPTER 1: General introduction…….. 1
1.1 Scope of this study…… 2
1.2 Fundamental physical properties of (La,Pr)$CaMnO_3$ …… 5
1.3. Optical measurements for study the physical properties of manganites …… 8
1.4. Nanopeculiar property in (La,Pr)$CaMnO_3$ nanostructures…… 10
1.5 References …… 12
CHAPTER 2: Experiment…… 15
2.1 Sample preparation…… 16
2.1.1 Pulsed laser deposition technique…… 16
2.1.2 Nanoimprint lithography …….. 18
2.2 Characterization …… 21
2.2.1 X-ray diffraction measurement …… 21
2.2.2 Electrical measurement …… 22
2.2.3 Hard X-ray photoemission spectroscopy …… 22
2.2.4 Terahertz time domain spectroscopy…….. 23
2.3 References…… 27
CHAPTER 3: Electrical transport properties through the metal insulator transition in the phase-separated (La,Pr,Ca)MnO_3 film investigated by the THz Time Domain Spectroscopy …… 29
3.1 Introduction …… 30
3.2 Purpose …… 32
3.3 Results …… 32
3.3.1 Sample preparation and crystal quality …….. 32
3.3.2 THz-TDS measurement …… 33
3.3.2.1 The transmitted THz waveforms…… 34
3.3.2.2 One media approximation …… 36
3.3.2.3 Temperature dependent THz conductivity… 38
3.4 Discussion …… 39
3.4.1 The Insulator-Metal Composite model…… 39
3.4.1.1 THz conductivity for mixed-phase material.. 39
3.4.1.2 Drude model for metal …… 40

3.4.1.3 Austin-Mott model for insulator …. ……... 41
3.4.1.4 Insulator-Metal Composite model.… ……... 42
3.4.2 Electrical transport properties……..……..…….. 44
3.5 Conclusion ….…...…….……...……...…….…..… 49
3.6 References ….…...…….……...……...…...……. 50
CHAPTER 4: Electrical transport properties in phase-separated $(La,Pr,Ca)MnO_3$ nanowires investigated using THz time domain spectroscopy ..…. ..……..…... 53
4.1 Introduction …….…….……...……..…….. 54
4.2 Purpose …….…….……...…….....…… 57
4.3 Experiment …….…….……...……..……... 57
4.4 Results and Discussion ….……...……...……. 59
4.4.1 The LPCMO nanowires strcutrure …..……...……. 59
4.4.2 The structure effect in LPCMO nanowires sample … 60
4.4.3 Electrical transport properties of LPCMO nanowires sample…….……...……...……... 63
4.4.4 Nanopeculiar properties of LPCMO nanowires sample ….……...……...……..….. 65
4.5 Conclusion ….…...…….……...……...……..….. 68
4.6 References ….…...…….……...……...…….…… 69
CHAPTER 5: Colossal magnetoresistive $(La,Pr,Ca)MnO_3$ nanobox array structures constructed by the three-dimensional nanotemplate pulsed laser deposition technique ……...…... 71
5.1 Introduction ….…...…….……...……..…..…… 72
5.2 Purpose …….…….……...…….....…… 73
5.3 Experiment ….…...…….……...……...…..…….. 73
5.4 Results and Discussion ….……...……...…..……... 75
5.4.1 Highly crystallized and precisely-size-controlled LPCMO nanoboxes……...……...…..……..... 75
5.4.2 Conductivity properties of LPCMO nanoboxes investigated uing Mn 2p core-level spectra ……... 77
5.4.2.1 Conductivity properties of LPCMO film….. 77
5.4.2.2 Conductivity properties of LPCMO nanoboxes……...……..... 82
5.5 Conclusion ….…...…….……...……...……... 84
5.6 References ….…...…….……...……..... 85
CHAPTER 6: General conclusion ……...……...…..…….. 87
CHAPTER 7: Appendix …...…….……...……...…..…….. 91

7.1 Analyzing procedure…… 92
7.2 Analyzing code …….. 93
List of publications …… 105
Acknowledgments …….. 109

CHAPTER 1

General introduction

1.1 Scope of this study

The separated electronic phases in 3d transition metal oxides originate from a strong correlation among electrons. The transition of these phases leads to the rich and exotic functionalities such as the colossal magnetoresistivity (CMR) in manganites [1,2], or the high-T_C superconductivity in cuprates [3]. In a typical perovskite manganite (La,Pr,Ca)MnO_3, it is observed that CMR is associated with the huge order-of-magnitude insulator-metal transition (IMT) [4] from an insulator behavior at a high temperature to a metallic behavior at a low temperature through a critical transition temperature by the coexistence of the separated domains in a nanometer scale. The spatial distribution of these domains is strongly associated with the observed conductivity behavior of the whole system. Therefore, the investigation of correlation between them is important to understand the IMT. Interestingly, as the electronic domains were confined in a limited area of a nanostructure, the nano-peculiar functionalities were observed [4], leading to a wonderful potential for applications in nanoelectronics devices.

So far, it is difficult to obtain the domain distribution or domain evolution using the electrical transport measurement with attached electrodes, even though this technique has been widely used to investigate the dc conductivity behavior. On the other hand, some observations of the phase-separated domains were achieved by microscope techniques, for examples, the transmission electron microscopy [5], the scanning tunneling microscopy [6], or by the mapping from photoemission techniques [7]. However, the requirements to conduct these types of microscopy experiments are extremely strict, for examples a nice surface in the scanning tunneling microscope, the limitation of samples' shape and size in TEM, or the difficulty to control the

measurement conditions. Hence, the realization of a technique to study the strong correlation of domain evolution and dc conductivity is required. This can be fulfilled by using the optical spectroscopy since the observed optical signal is proportional with the domain distribution and their corresponding conductivity properties. With the development of THz spectroscopy, such as terahertz time domain spectroscopy (THz-TDS), the investigation of the conductivity behavior was partially explained based on the existing models such as the Drude model for free electrons' conductivity in metal [8] and the Austin-Mott model for the hopping conductivity through localized states in insulator [9]. However the simultaneous investigation of domain evolution and dc conductivity in the phase separated condition was not realized due to the lack of a comprehensive model to explain the change in conductivity behavior through IMT in this composite material.

The originality of this study is the establishment of a procedure to investigate the electrical transport properties, including the domain evolution (temperature dependence of metal fraction $X(T)$) and the dc conductivity $\sigma_{dc}(T)$ of a typical nanoscale phase-separated manganite (La,Pr,Ca)MnO_3 by using terahertz time domain spectroscopy (THz-TDS). The general introduction on the scope of this research and some fundamental properties of this specific composite material is presented in Chapter 1. The experiment techniques I employed to fabricate and characterize the samples are introduced in Chapter 2. Chapter 3 exhibits the initial approach to study electrical transport properties of a phase-separated bulk system using THz-TDS. In this chapter I proposed a composite model to explain the changes in THz conductivity curve ($\sigma_{THz}(\omega,T)$) through the IMT. By fitting this model with the obtained $\sigma_{THz}(\omega,T)$ curves, I could simultaneously obtain the domain evolution $X(T)$ and dc conductivity

$\sigma_{dc}(T)$ for a (La,Pr,Ca)MnO_3 film. Next, I employed this technique to nanostructures. The demonstration for a (La,Pr,Ca)MnO_3 nanowires sample is presented in Chapter 4. To obtain the enough signal/noise ratio for the (La,Pr,Ca)MnO_3 nanowires sample, I employed a nanoimprint-based technique to fabricate the high density nanowires sample over a large area. To obtain the intrinsic conductivity behavior, I successfully excluded the structure effect originating from the polarization of THz pulse and the wire alignment. The metal fraction $X(T)$ and dc conductivity $\sigma_{dc}(T)$ for this nanowires sample could be obtained by fitting the composite model with their $\sigma_{THz}(\omega,T)$ curves without attaching electrodes. As a development of nanostructure fabrication, I successfully fabricated the (La,Pr,Ca)MnO_3 nanoboxes with the precise control of the wall-width down to 30 nm using an original three-dimensional nanotemplate pulsed laser deposition technique. The results on this part will be introduced in chapter 5. Finally, in chapter 6, I summarized all the achievements and suggested the potential for application of this technique to investigate electrical transport properties ($X(T)$ and $\sigma_{dc}(T)$) for other composite materials with variety of shape, size, and structure such as the core-shell semiconductor nanocrystals, the high-temperature alloy resistor, and variety of heterostructures without concerning for attaching electrodes.

1.2 Fundamental physical properties of (La,Pr)CaMnO$_3$

Perovskite manganite (La,Pr,Ca)MnO$_3$ is a typical strongly correlated electrons material with the fascinating colossal magnetoresistance [10-21] which associates with the huge-order-of-magnitude metal-insulator or insulator-metal transition (MIT/IMT) as shown in figure 1.1. In this material, the transition property can be modulated by applied external fields such as the temperature, and so on. At a low temperature and/or a high magnetic field, the temperature dependent resistance ($R(T)$) curves presented the metallic behavior and then changed to the insulator behavior at a high temperature and/or a low magnetic field. The transition appeared at a critical temperature T_{MI} in the heating, or T_{IM} in the cooling process.

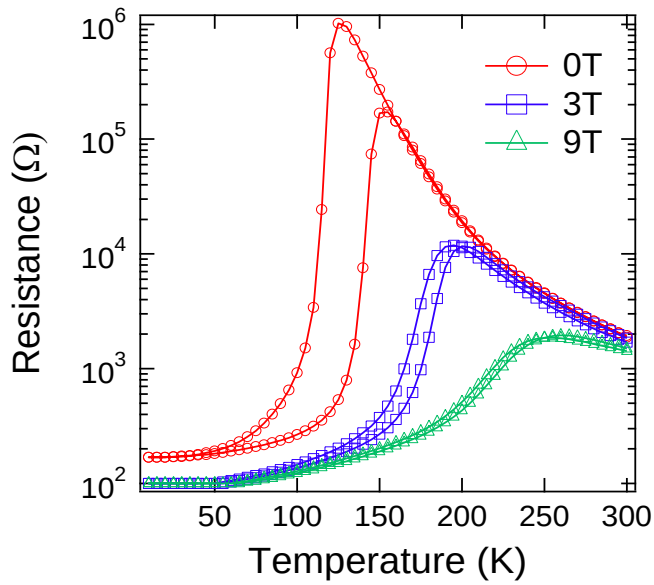

Fig. 1.1: MIT/IMT property in a typical (La,Pr,Ca)MnO$_3$ system (unpublished data).

Interestingly, in the IMT process of (La,Pr,Ca)MnO$_3$, the coexistence of metallic and insulator domains has been reported. Historically, the possibility of "electronic" phase separation was already discussed in the theoretical works of Nagaev [22,23] using one orbital model for an antiferromagnetic semiconductor

embedded with ferromagnetic regions. Also some calculations were performed for the manganites [24,25]. Experimentally, the inhomogeneities in manganites were observed using different techniques such as the electron microscopy [5], the scanning tunneling spectroscopy [6], the neutron scattering [26], or the mapping from photoemission techniques [7], and the scanning electron microscopy cathodoluminescent [4], and so on. Even though the observations of phase-separated domains were achieved at a certain level as shown in Fig. 1.2, it should be noted that the conditions to conduct these types of mentioned-above experiments are extremely strict, for examples nice surface in the scanning tunneling microscope, the limitation of samples' shape and size in TEM, or the lack of resolution in mapping techniques.

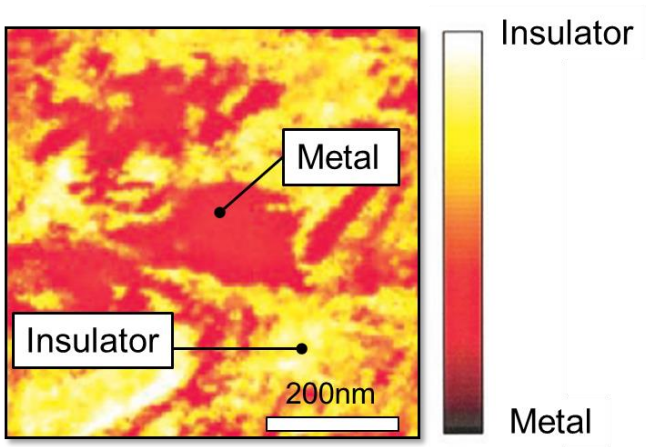

Fig. 1.2: Scanning tunneling spectroscopy image of phase-separated (La,Ca)MnO_3.[6]

It is widely agreed that the observed conductivity behavior is determined by the spatial distribution of metal and insulator domains and their corresponding conductivity properties. As a result, many researchers have paid much effort in unveiling the relationship between the observed conductivity behavior and the spatial distribution of domains. For example, L. Zhang *et. al*,[27] combined the domain distribution images of $(La_{0.33}Pr_{0.34}Ca_{0.33})MnO_3$ obtained by magnetic force microscopy (in both cooling (A) and heating (C) process) with the resistivity curve

obtained from electrical probe measurement as shown in figure 1.2.3. The temperature-induced evolution of ferromagnetic metallic domains in A and C graphs were firmly related to the conductive behavior in the B graph. However, the separate investigations of domain distribution and conductivity behavior made the comparison difficult. Hence, the simultaneous estimation of domain revolution and dc conductivity is required.

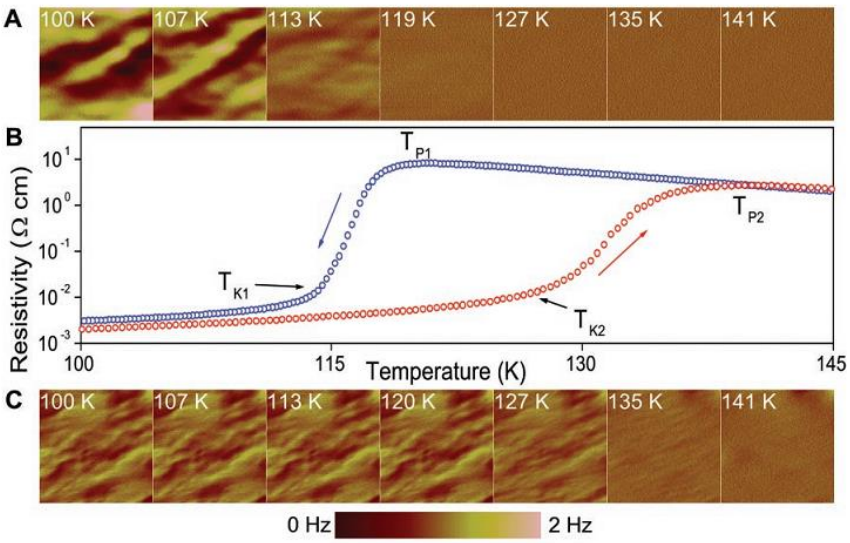

Fig. 1.3: Temperature dependent magnetic force microscopy images of $(La_{0.33}Pr_{0.34}Ca_{0.33})MnO_3$ in both cooling (A) and heating (C) process. Temperature dependent resistivity curve was shown in (B). [27]

1.3 Optical measurements for study the physical properties of manganites

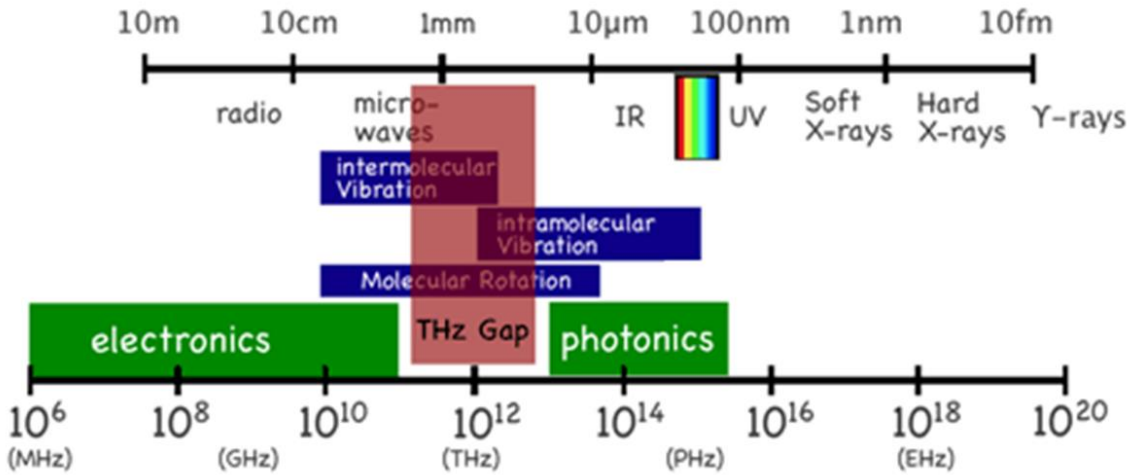

Figure 1.4: Electromagnetic spectrum.

So far, the study of optical response of strongly correlated electron materials is an efficient tool to investigate their physical properties thanks to the variety of electromagnetic waves as shown in Fig. 1.4. For examples, the investigation of systematic variation of the electronic structure in La*M*O_3 (*M* is a transition metal) was obtained using a long range of photon energy from 0.015 eV in the infrared (IR) region to 36 eV in the soft X-rays region [28]; and the relationship between electric and magnetic states in (La,Ba)MnO_3 system was unveiled using hard X-ray photoelectron spectroscopy [29]. To understand the low-energy electrodynamic response of electrons near Fermi-level in the manganites, the terahertz spectroscopy, such as terahertz time domain spectroscopy (THz-TDS) was employed [8-9]. R. Rana explained the metallic behavior in the THz conductive curve of (Pr,Sr)MnO_3 film (Fig. 1.5 (a)) by the Drude model [8] and K. R. Mavani explained the insulating behavior in (Nd,Ca)MnO_3 film (Fig. 1.5 (b)) with the power law increase of THz conductivity [9] following Austin-Mott model. However, there is no effort to explain the change of THz conductivity behavior through the IMT process.

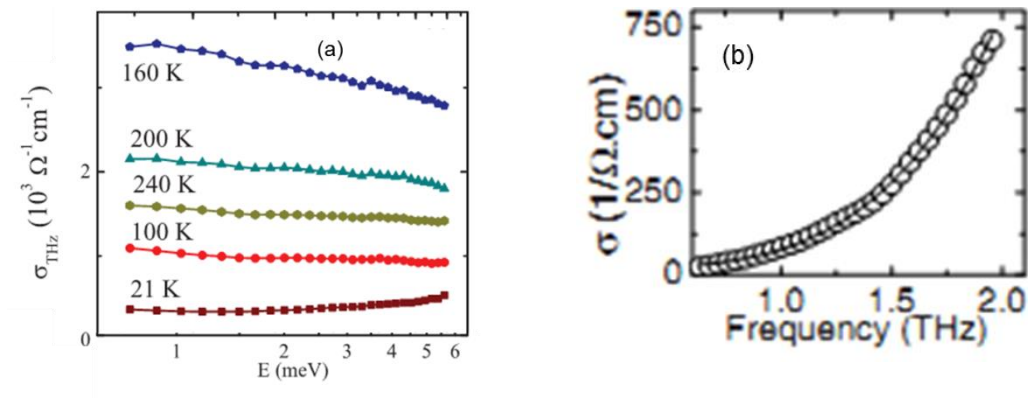

Fig. 1.5: THz energy/frequency dependence of conductivity in (a) (Pr,Sr)MnO_3 with the Drude behavior [8], and (b) (Nd,Ca)MnO_3 with [29] (1 THz ≈ 4.14 meV).

For a phase-separated manganite with the coexistence of insulator and metal domains, the domain distribution (corresponding to the metal fraction *X*) and conductivity behavior of each phase (σ^I for insulator phase and σ^M metal phase) would be obtained thanks to the observed THz conductivity $\sigma_{THz}{}^{\text{observed}}$ from THz-TDS measurement, since the observed THz pulse passing through the sample is proportional to values of *X*, σ^I, and σ^M (illustrated in Fig. 1.6).

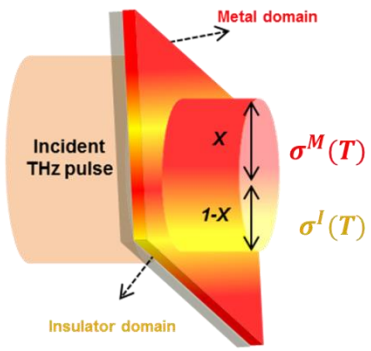

$$\boldsymbol{\sigma_{THz}}^{\text{observed}} = (\mathbf{1} - \boldsymbol{X(T)})\boldsymbol{\sigma^I(T)} + \mathbf{X}\boldsymbol{\sigma^M(T)}$$

Figure 1.6: Schematic illustration for the potential of THz-TDS in simultaneous investigation of domain distribution and conductivity.

To analyze this relationship, a comprehensive model should be proposed to thoroughly explain the change in $\sigma_{THz}{}^{\text{observed}}$ behavior. This is unsolved important

issue in THz-TDS measurement, thus an establishment of this method will give a big progress in the spectroscopic research field.

1.4 Nanopeculiar property in (La,Pr)$CaMnO_3$ nanostructures

Generally in the SC electron materials, the spatial phase inhomogeneity of electronic domains in a nanometer scale and the interplay between them usually lead to the rich and fascinating properties such as the high-T_C superconductivity, the colossal magnetoristance, and so on. However, the investigation of fundamental properties of these materials has been hampered due to an averaged response of the inhomogeneous ensembles to external parameters in the multiple domain structures of large-scale samples such as a film. By confining the nanoscaled electronic domains in a limited area of a microstructure or a nanostructure, the peculiar properties have been obtained and some hidden physical mechanisms have been revealed.

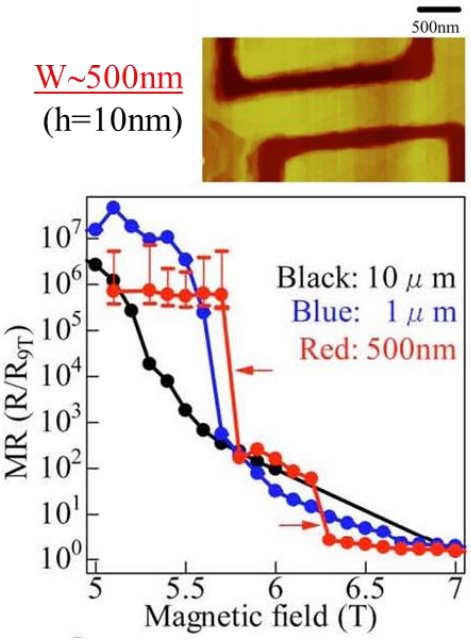

Fig. 1.7: Magnetic field dependence of magnetoresistance in LPCMO channel with different channel width. [30]

In the case of the (La,Pr,Ca)MnO_3 system, efforts in investigation of superior features in down-sized structures have been conducted. Figure 1.7 shows the magnetoresistance of a (La,Pr,Ca)MnO_3 channel with the different channel width in which the extremely sharp transition from the insulator property to the metallic feature was observed in a 500-nm-width channel, while only the gradual transitions were observed in the 1-μm-width and 10-μm-width ones. Thanks to the confinement of electronic regions in the sub-micrometer scale to the several ten nanometer scale, the insulator domain was trapped in the nanochannel even under a certain magnetic field condition which acted as a “bottle neck” area in preventing the conduction path between electrodes. The sudden transition in this 500-nm-width channel was attributed to the transition of the single trapped insulator domain to the metallic state. This investigation suggested that the nanostructuring is a new and good way to realize high sensitive oxide nanodevices as the purpose of this study. The investigation of electrical transport properties without attaching electrodes is also a scope of this thesis.

1.5 References

1. A. P. Ramirez, J. Phys.: Condens. Matter **9** (1997) 817
2. J. M. D. Coey, M. Viret, and S. von Molnár, Adv. Phys. **48** (1999) 167
3. M. K. Wu, J. R. Ashburn, C. J. Torng, P. H. Hor, R. L. Meng, L. Gao, Z. J. Huang, Y. Q. Wang, and C. W. Chu., Phys. Rev. Lett. **58** (1987) 908
4. A. N. Hattori, Y. Fujiwara, K. Fujiwara, T. V. A. Nguyen, T. Nakamura, M. Ichimiya, M. Ashida, H. Tanaka, Nano letters, **15** (2015) 4322
5. M. Uehara, A., Mori, C. H., Chen, S.-W., Cheong, Nature **399** (1999) 560.
6. M. Fäth, S. Freisem, A. A. Menovsky, Y. Tomioka, J. Aarts, J. A. Mydosh, Science **285** (1999) 1540
7. D. D. Sarma, D. Topwal, U. Manju, S. R. Krishnakumar, M. Bertolo, S. La Rosa, G. Cautero, T. Y. Koo, P. A. Sharma, S.-W. Cheong, A. Fujimori, Phys. Rev. Lett. **93** (2004) 097202
8. R. Rana, P. Pandey, D. S. Rana, K. R. Mavani, I. Kawayama, H. Murakami, M. Tonouchi, Phys. Rev. B **87** (2013) 224421
9. K. R. Mavani, M. Nagai, D. S. Rana, H. Yada, I. Kawayama, M. Tonouchi, K. Tanaka,Appl. Phys. Lett. **93** (2008) 231908
10. E. Dagotto, T. Hotta, A. Moreo, Physics Reports 344 (2001) 1
11. H. Y. Hwang, S-W. Cheong, P. G. Radaelli, M. Marezio, B. Batlogg, Phys. Rev. Lett. **75** (1995) 914
12. Y. Tokura, ed., *Colossal Magnetoresistance Oxides*, Gordon and Breach Science Publishers, London (2000)
13. P. Schieffer, A. P. Ramirez, W. Bao, S-W. Cheong, Phys. Rev. Lett. **75** (1995) 3336

14. M. Uehara, S. Mori, C. H. Chen, S-W. Cheong, Nature **399** (1999) 560

15. Y. Tokura, Physics Today, July 2003, 50

16. H. Y. Hwang, S-W. Cheong, Contribution to Colossal Magnetoresistance Oxides (Y. Tokura, ed.), Chapter 7 : Monographs in Condensed Matter Science. Gordon & Breach, London 1999

17. D. S. Dessau, Z.-X. Shen, Part 5 : Direct electronic structure measurements of the colossal magnetoresistive oxides, Colossal magnetoresistive oxides, Ed. Y. Tokura, Gordon and Breach Science Publishers, 2000

18. P. W. Anderson and H. Hasegawa, Phys. Rev. **100** (1995) 675

19. A. Millis, B. I. Shraiman, R. Mueller, Phys. Rev. B **54** (1996) 5389

20. A. Millis, B. I. Shraiman, P. B. Littlewood, Phys. Rev. Lett. **74** (1995) 5144

21. J. Kanamori, Prog. Theor. Phys. **30** (1963) 275

22. E. L. Nagaev, JETP Lett. **6** (1967) 18

23. E. L. Nagaev, Sov. Phys. Lett. **27** (1968) 122

24. L. Sheng, D. Y. Xing, D. N. Sheng, C. S. Ting, Phys. Rev. Lett. **79** (1997) 1710

25. A. Yunoki, A. Moreo, Phys. Rev. B **58** (1998) 6403

26. J. M. De Teresa, C. Ritter, M. R. Ibarra, P. A. Algarabel, J. Garcia-Munoz, J. Blasco, J. Garcia, C. Marquina, Phys. Rev. B **56** (1997) 3317

27. L. Zhang, C. Israel, A. Biswas, R. L. Greene, A. de Lozanne, Science **298** (2002) 805

28. T. Arima, Y. Tokura, Journal of the Physical Society of Japan **64** (1995) 2488

29. S. Ueda, H. Tanaka, E. Ikenaga, J. J. Kim, T. Ishikawa, T. Kawai, K. Kobayashi, Phys. Rev. B **80** (2009) 092402

30. Y. Yanagisawa, H. Tanaka, T. Kawai, Appl. Phys. Lett. **89** (2006) 253121

CHAPTER 2

Experiment

2.1 Sample preparation

In my research, the samples such as the (La,Pr,Ca)MnO_3 film, microwires, nanowires, nanoboxes were prepared by the pulsed laser deposition (PLD) combined with nanoimprint lithography. The details of experimental methods are described in the following parts.

2.1.1 Pulsed laser deposition technique

Pulsed laser deposition (PLD) is a technique for the thin film deposition in which a high-power pulsed laser beam is focused on a target of materials inside a high vacuum chamber [1]. Historically, this technique has been first applied by Smith and Turner [2] in 1965 for the fabrication of semiconductors and dielectric thin films. The breakthrough for PLD had been made in 1987 [3] with a high quality thin film of a high temperature superconductive material $YBa_2Cu_3O_7$ which was superior to films deposited by other techniques. These works already showed main characteristics of PLD, namely the stoichiometry transfer between target and deposited film, high

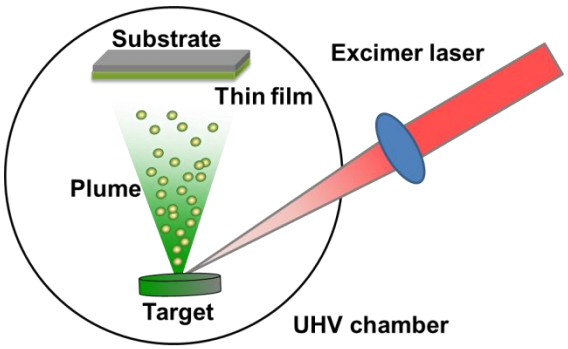

Fig. 2.1: A typical set-up for a pulsed laser depostion.

deposition rates of about 0.1 nm per pulse. Since then, the PLD technique has been used to grow various types of high quality crystalline films of oxides, nitrides, or fabricate metallic multilayers, superlattices. In the 1990s the development of new

laser technology, such as lasers with high repetition rate and short pulse durations, leaded to the ability for the growth of well-defined films with complex stoichiometry.

A typical set-up for PLD is schematically illustrated in Figure 2.1. In an ultra-high vacuum (UHV) chamber, the surface of a desired target material has been struck by a high-power pulsed laser beam, which leads to the evaporation of the material as a plume. The ablated atoms or ions, molecules are deposited on a substrate where their reconstruction has been done. In the PLD process, the laser energy, the working pressure and the ambient atmospheres such as oxygen, nitrogen can be selectively chosen in order to reproduce the exact stoichiometry of a complex materials system.

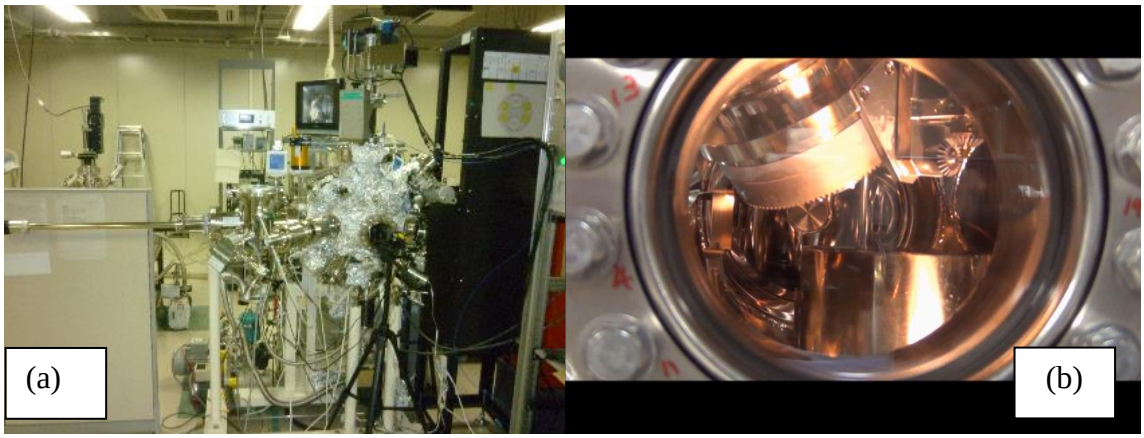

Fig. 2.2: **(a)** The image of the 3D-PLD system; **(b)** The substrate holder has been inclined (e.g., here is 60°) inside the UHV chamber.

In my study, the LPCMO thin film, nanowires and nanoboxes have been fabricated using PLD process. Figure 2.2 (a) shows a photo of our original PLD chamber, called 3D-chamber. This special name originated from its ability for fabricating the three-dimentional (3D) nanostructures such as nanowires, nanoboxes, and so on. The key advantage of this chamber is that the deposition angle can be controlled from 0° to 60° as shown in Fig. 2.2 (b). The azimuth angle of the substrate

has been circularly rotated. The base pressure of the chamber was maintained to less than 1×10^{-6} Pa. An excimer laser L28-18-1/2 (Lambda Physik, USA) with ArF radiation (wavelength 193 nm) was used. The laser fluence was about 2 mJ/cm^2.

In my research the LPCMO nanostructures such as the nanobox array structures and nanowires have been constructed using our newly established nanofabrication technique called three-dimensional (3D) nanotemplate pulsed laser deposition (PLD) technique [4-7]. This is the combination of the PLD technique with the nano imprint lithography (NIL) technique. Figure 2.3 shows the schematic illustration of a typical fabrication process for LPCMO nanoboxes using 3D nanotemplate PLD technique. The key point of this method is that we still could employ advantages of a thin film deposition using PLD which enabled us to produce highly crystallized nanostructures while maintaining initial template positions and shapes of the resist patterns obtained from NIL exactly on a large area.

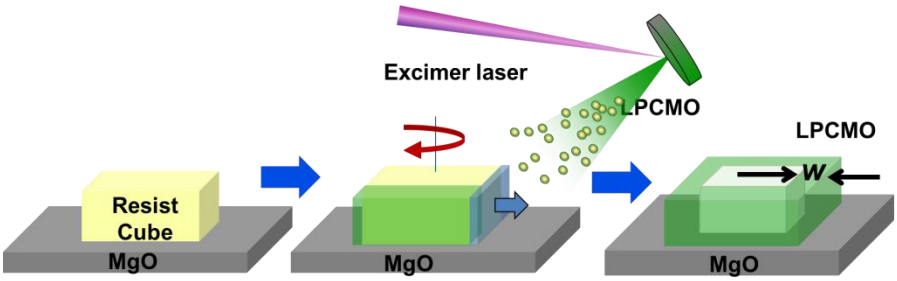

Fig. 2.3: Schematic illustration of the fabrication procedure of the LPCMO nanoboxes using the three-dimensional (3D) nanotemplate pulsed laser deposition (PLD) technique.

2.1.2 Nanoimprint lithography

Nanoimprint lithography (NIL) is a technique to fabricate the nanometer-scale patterns. Historically NIL has been first appeared in scientific literature since 1996 [8]

and then this technique has been developed with different variations and implementations. This is a nonconventional lithographic technique with a lot of advantages such as the low cost, high-throughput, and high resolution. Traditionally, a lithographic technique such as ultra-violet (UV) lithography or electron beam lithography can achieve a pattern through the modification of the chemical and physical properties of a resist after excitation of the photons or electron beam. So the resolution of this technique is set by the light diffraction or beam scattering. This limitation can be overcome by using NIL technique by which, the nanostructured patterns have been created by a mechanical deformation of an imprint resist. The imprint resist is typically a monomer or polymer formulation that is cured by heat or UV light during the imprint.

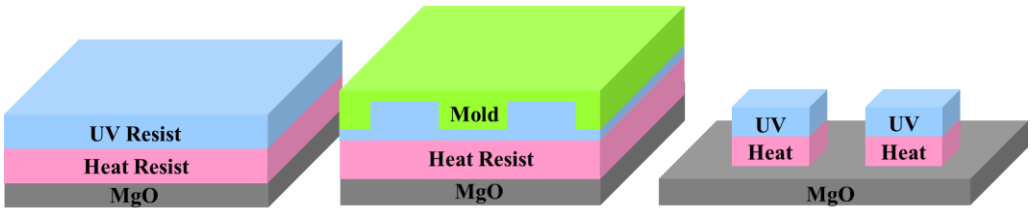

Fig. 2.4: Schematic image of the nanoimprint lithography technique.

Schematic image of a fabrication of nanoboxes template resist pattern using the nano imprint lithography technique is shown in figure 2.4. At first, two layers of a bottom thermally curable resist (NXR-3032-4%, Nanonex, USA) and a top UV curable resist (NXR-2030-8%, Nanonex, USA) were covered on an MgO substrate by spin coating method. Depend on the depth and the size of the cavities in the mold, the volume of resist and the condition for spin coating have been adjusted. Soon after that, by using a nano imprinter (Entre 3, Obducat, Sweeden), the UV Nano Imprint Lithography was carried out at room temperature under the pressure of 30 bar for transferring the pattern from a quartz mold (NTT-AT Nanofabrication Corporation,

Japan) into the UV curable resist layer with the expose of UV light. In this process, the viscous UV curable resist was forced to flow into the cavities of the mold, so the polymer rheology issues should be taken into account when optimizing the pressing process. The separation between the mold and resist pattern was manually conducted. For high aspect ratio structures or/and high density structures, this process becomes a critical step in the replication process in which adhesions or imperfections of the nanostructures tend to occur due to the high friction between mold and resist. To reduce friction forces, the anti-sticking treatment was conducted for the mold using a chemical solution Optool HD1100TH (DAIKIN, Japan). In the next step, the two-step reactive ion etching process was employed (RIE-10NOU, Samco, Japan) in order to get the cube-like template pattern using CF_4 and O_2 ions, respectively. The UV resist layer was removed by CF_4 plasma at 10 sccm, 2 Pa, 50 W in 2 minutes. The heat resist was etched by O_2 plasma at 10 sccm, 2 Pa, 50 W in 2 minutes. Figure 2.5 (a) and (b) shows the images of NIL and RIE systems employed in the nanotemplate preparation process.

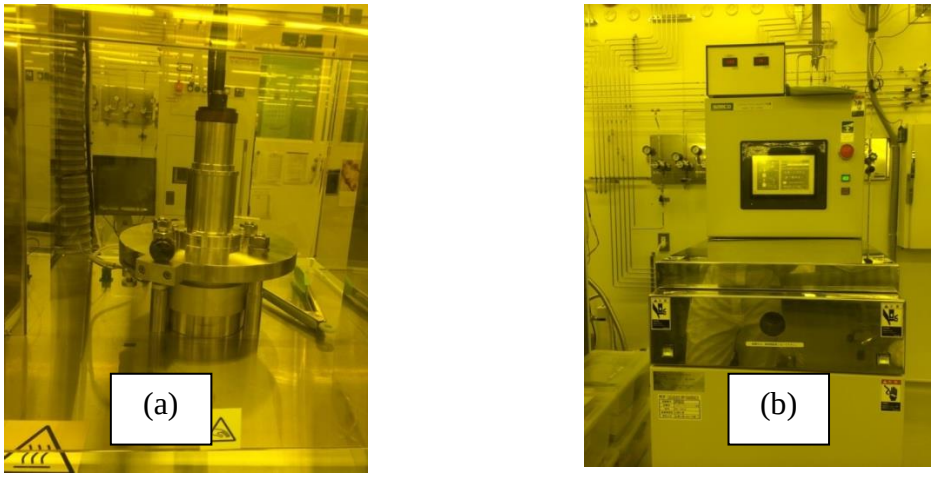

Fig. 2.5: (a) Nano Imprint Lithography system, Eitre 3, 030-5065, Obducat AB, Sweeden; (b) Reactive ion etching system, RIE-10NOU, Samco, Japan.

2.2 Characterization

In my research, the various characterization techniques were employed for samples. For examples, the crystal quality was characterized by X-ray diffraction, the geometry and topography were checked by Scanning Electron Microscope and Atomic Force Microscope, the electrical transport properties are investigated using terahertz time domain spectroscopy, and so on. The details of characterization methods are described in the following parts.

2.2.1 X-ray diffraction measurement

The first X-ray diffraction (XRD) on copper sulfate crystal was conducted by Max von Laue in 1912. After this pioneering research, the XRD experiment developed rapidly and now becomes an effective and common technique to study crystal structures and atomic spacing of materials. As the X-ray comes to a crystal, a regular array of scatters (electrons in atoms) produces a regular array of spherical waves which cancel one another out in most directions through destructive interference and some constructive interfere in a few specific directions determined by Bragg's law: $2d\sin\theta = \mathrm{n}\,\lambda$, here d is the spacing between diffracting planes; θ is the incident angle; n is an integer; and λ is the wavelength of the X-ray. By using X-ray with a certain wavelength λ, the value of d can be estimated base on the diffraction peaks at corresponding angle θ.

In my study, the 2θ-θ scan was performed for all LPCMO film, microwires, nanowires, nanoboxes samples by using an X-ray diffraction apparatus (Smart Lab, Rigaku, Japan)) at room temperature. The Cu-Kα line (λ = 0.15405 nm) was used for the measurements.

2.2.2 Electrical measurement

In my research, the dc electrical conductivity was measured by the four-probe method with a source-meter unit (2612A, Keithley Instruments) in a He-flow cryostat (temperature range was from 10 K to 300 K). Electrodes used for electrical measurements were fabricated from an electron-beam-deposited bilayer film of Ni/Au (thickness of about 5 nm/50 nm). All of the measurement apparatus was controlled using LabVIEW system (National Instrument).

2.2.3 Hard X-ray photoemission spectroscopy

Photoemission spectroscopy (PES) is a powerful technique to experimentally determine electronic structure of core levels and valence bands of materials. Conventional PES and even soft X-ray PES, however, are very sensitive to the sample's surface because of short inelastic mean free paths. This made it rather difficult to probe bulk character of material. To attain larger probing depths, the hard X-ray photoemission spectroscopy (HX-PES) was first conducted by Lindau in 1974 using a 1st generation synchrotron radiation (SR) [9]. Since then, a lot of effort has been paid to obtain the high-energy resolution, high throughput by using high-brilliance SR from 2nd generation and 3rd generation SR; and a high performance electron energy analyzer.

In my research, the HX-PES experiment was conducted at the undulator beamline BL15XU [10] of SPring-8 with the excitation photon energy of 5950 eV. The total energy resolution was 230 meV. The measurement temperature was ranged from 20 K to 300 K.

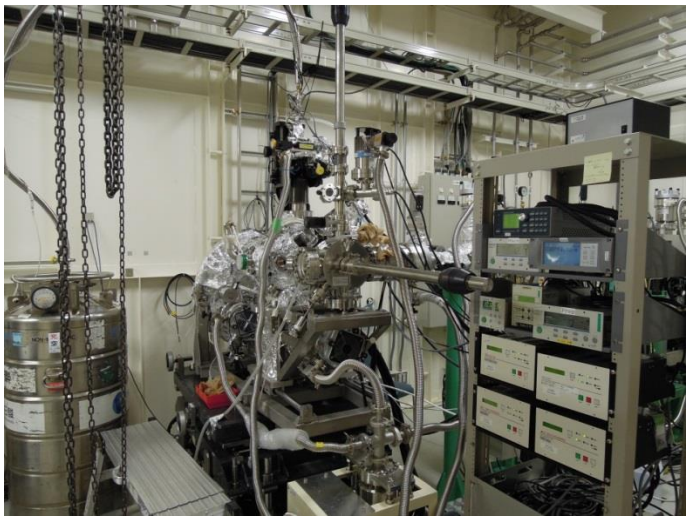

Fig. 2.6: The image of the hard Xray photo emission spectroscopy system inside beamline BL15XU.

2.2.4 Terahertz time domain spectroscopy

Terahertz time domain spectroscopy (THz-TDS) is a spectroscopic technique in which the properties of a material for examples complex refractive index, or complex dielectric constant are probed by using short pulses of terahertz radiation. The obtained THz pulses after passing through the material will have amplitude change and phase shift associated with the material's physical properties. Thus this technique can provide more information than conventional Fourier-transform spectroscopies which only reveal the change in amplitude [11,12].

The THz pulses can be generated using different ways such as from a photoconductive antenna or a nonlinear crystal after excited by an ultrashort pulse. The photoconductive (Auston) antenna or a nonlinear crystal can be used for detection of a THz pulse with an electro-optical sampling method (Pockels effects) using an ultrashort pulsed laser. Figure 2.7 (a) presents a photoconductive switch which consists of a semiconductor bridging a gap in a transmission line structure deposited

on the semiconductor substrate. Figure 2.7 (b) illustrates the response of the voltage-biased photoconductive switch to a short optical pulse focused onto the gap between the two contacts.

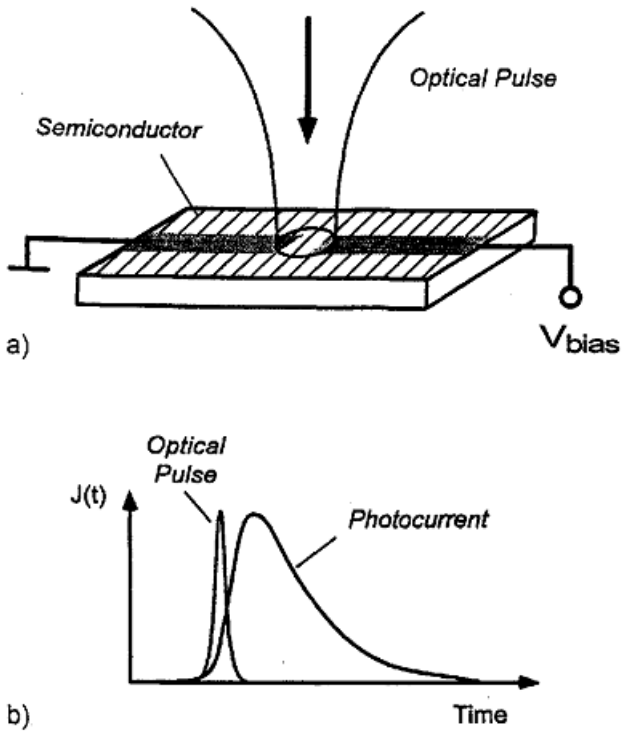

Fig. 2. 7: (a) Schematic of a photoconductive "Auston" switch with a transmission line. Optical pulsed are focused onto the gap in the transmission line and inject carriers into the semiconductor, leading to a current transient *J*(t) flowing across the gap in the line. (b) Typical current respond *J*(t) of a photoconductive switch to a short optical excitation pulse. [12]

The current through the switch rises very fast after injection of photocarriers by the optical pulse, and then decays with a time constant depending on the carrier lifetime of the semiconductor. The transient photo current *J*(t) radiates THz pulse into free space as shown in Eq. (2.1) (according to the Maxwell's equations):

$$E_{\mathrm{THz}}(T) \sim \frac{\delta J(\mathrm{t})}{\delta t} \qquad (2.1)$$

To use the Auston switch as a detector of a short electrical pulse, a current-to-voltage amplifier (ammeter) is connected across the photoconductor, replacing the voltage bias. The electric field of an incident THz pulse now provides the driving field for the photocarriers. Current flows through the switch only when both the THz field and photocarriers are present. Since electronics are not fast enough to measure the THz transients directly, repetitive photoconductive sampling is used. Typically, a generated THz pulse last only a few picoseconds, after passing through the material, the THz pulse with certain amplitude of electric field will interacts in the detector with a much-shorter laser pulse (~ 0.1 picoseconds) in a way that produces an electrical signal. This signal is proportional to the electric field of the THz pulse at the time corresponding to the time the laser pulse gates the detector on. This procedure is repeated and by tuning the timing of the gating laser pulse, it is possible to scan the THz pulse and construct its electric field as a function of time. Then, a Fourier transform is used to extract the frequency domain spectrum.

In my research, the THz-TDS experiments were conducted in Prof. Ashida Lab of Graduate School of Engineering Science, Osaka University. The schematic image for the THz-TDS set-up is shown in figure 2.8. Here, I used optical pulses from a mode-locked Ti:sapphire laser (Tsunami, Spectra Physics Inc. Ltd.) with a repetition rate of 80 MHz and an average power of 400 mW. The center frequency of the laser was 800 nm with the pulse duration (full width at half maximum) of 18 fs, which was split into two beams. One of the beams was focused on a GaAs photoconductive antenna to generate coherent THz pulses. The backward emitted THz pulses were collected to minimize the GaAs substrate's absorption and dispersion, and focused onto another photoconductive antenna using four off-axis parabolic mirrors. The other

optical beam was used to sample the transmitted THz pulses and was also focused onto the same spot of the photoconductive antenna for the detection, and the current induced by the THz electric field was detected. By changing the time delay between the two pulses, the electric field amplitude of the THz pulses could be measured as a function of time. To improve the signal-noise ratio, we employed a fast-scan delay line with an optical delay amplitude of 15 ps at a repetition frequency of 20 Hz [11]. The measurements were performed in dry air, or in nitrogen to reduce the absorption peaks from H_2O molecules.

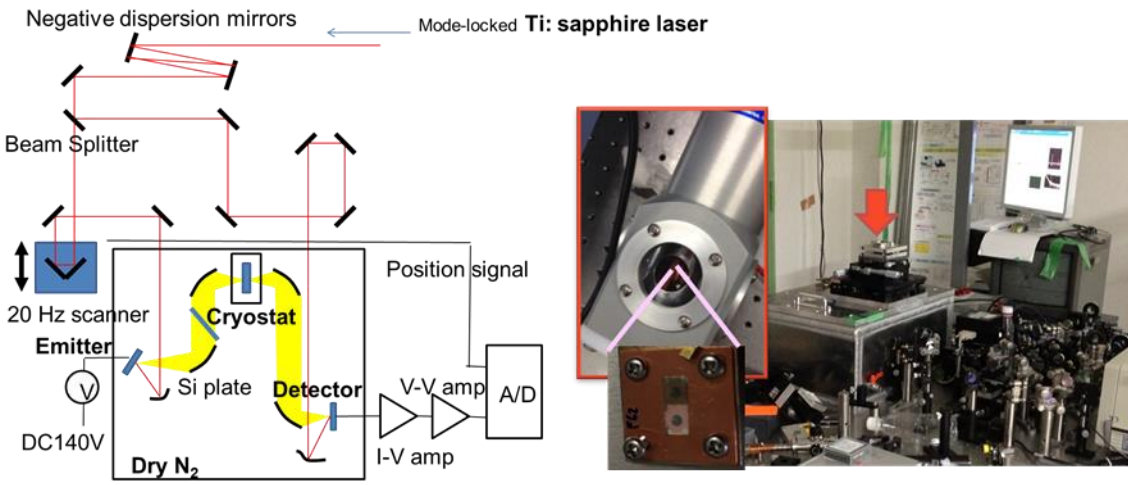

Fig. 2. 8: Schematic of the terahertz time domain spectroscopy set-up (left); and the actual THz-TDS set-up (right).

2.3 References

1. Pulsed Laser Deposition of Thin Films, edited by Douglas B. Chrisey and Graham K. Hubler, John Wiley & Sons, 1994 ISBN 0-471-59218-8
2. H. M. Smith, A. F. Turner, Appl. Opt. **4** (1965) 147
3. D. Dijkkamp, T. Venkatesan, X.D. Wu, S.H. Shaheen, N. Jisrawi, Y.H. Min-Lee, W.L. McLean, M.Croft, Appl. Phys. Lett. **51** (1987) 619
4. T. Kushizaki, K. Fujiwara, A. N. Hattori, T. Kanki, and H. Tanaka, Nanotechnology **23** (2012) 485308
5. A. N. Hattori, A. Ono, and H. Tanaka, Nanotechnology **22** (2011) 415301
6. A. N. Hattori, M. Ichimiya, M. Ashida, and H. Tanaka, Appl. Phys. Express **5** (2012) 125203
7. Y. Fujiwara, A. N. Hattori, K. Fujiwara, and H. Tanaka, Jpn. J. Appl. Phys. **52** (2013) 015001
8. S. Y. Chou, P. R. Krauss, P. J. Renstrom, Science **272** (1996) 5258
9. I. Lindau, P. Pianetta, S. Doniach, W. E. Spicer, Nature **250** (1974) 214
10. S. Ueda, Y. Katsuya, M. Tanaka, H. Yoshikawa, Y. Yamashita, S. Ishimaru, Y. Matsushita, and K. Kobayashi, AIP Conf. Proc. **1234** (2010) 403.
11. H. Shimosato, T. Katashima, S. Saito, M. Ashida, T. Itoh, K. Sakai, Phys. Stat. Sol. (c) **3** (2006) 3484
12. Milimeter and submilimeter wave spectroscopy of solids, Ed. G. Grüner, Springer, 1998

CHAPTER 3

Electrical transport properties through the metal insulator transition in the phase-separated $(La,Pr,Ca)MnO_3$ film investigated by the THz Time Domain Spectroscopy

Abstract

Temperature-dependent terahertz conductivities ($\sigma_{THz}(\omega,T)$) were obtained for a phase-separated $(La_{0.275}Pr_{0.35}Ca_{0.375})MnO_3$ (LPCMO) film using THz time domain spectroscopy. For understanding the change of $\sigma_{THz}(\omega,T)$ behavior, I proposed an insulator-metal composite model by incorporating Austin-Mott model characterizing the hopping of localized electrons and Drude model explaining the behavior of free electrons. This model well described $\sigma_{THz}(\omega,T)$ for a LPCMO film through the insulator-metal transition (IMT). Using this model, I could reliably investigate the electrical transport properties of the LPCMO film based on THz conductivity measurement, i.e., simultaneously evaluate the competing composition of metal and insulator phases and the dc conductivity through the IMT.

3.1 Introduction

Transition metal oxides are of particular interest since they exhibit numerous exotic properties, such as colossal magnetoresistance associated with the insulator-metal transition (IMT), originating from the strong electronic phase competition, observed in response to the changes under the applied external fields such as temperature, and so on [1-3]. For example, the typical perovskite manganite $(La,Pr,Ca)MnO_3$ exhibits a transition from the insulator phase at a high temperature to the metal phase at a low temperature [4-5]. In the temperature-induced IMT of $(La,Pr,Ca)MnO_3$, metal domains nucleate at seed points in a film, then grow and spread with decreasing temperature toward the transition temperature T_c [1,5]. Hence,

in the vicinity of T_c, the so-called coexistence region, the metal and insulator phases are both present. The domain revolution, i.e., the temperature-dependent population of the metal phase ($X(T)$), strongly affects the dc conductivity (σ_{dc}) of an phase-separated material [6]. The simultaneous investigation of σ_{dc} and $X(T)$ related to the IMT is important for the application of phase-separated materials to future nanoelectronic devices. This has remained challenging with conventional dc electrical conductivity measurements using attached electrodes, in which the total flow of the electrons among all domains at the Fermi level is measured as the conductivity. To realize a simultaneous evaluation, optical spectroscopy techniques are promising and have been employed for measurements of many transition metal oxide materials [7-14]. Among them, THz time domain spectroscopy (THz-TDS) is a powerful method that has been widely applied to various manganites to investigate their intrinsic conductivity $\sigma_{THz}(\omega)$ as well as their electronic structure in the vicinity of the Fermi level [7-9]. Many previous studies have obtained the temperature-dependent THz conductivity $\sigma_{THz}(\omega>0,T)$ for manganites at various frequencies [8,12]. However, challenges still remain in quantitatively estimating the temperature-dependent THz conductivity in the vicinity of 0 THz ($\sigma_{THz}(\omega\rightarrow 0,T)$), abbreviated to $\sigma_0(T)$, which is the dc conductivity $\sigma_{dc}(T)$ [9,14]. This is because of the lack of a physical model that conforms with the dramatic change in $\sigma_{THz}(\omega)$ behavior through the IMT. Also, to explain the $\sigma_{THz}(\omega)$ behavior, the Drude model [8,10] for metallic samples and the Austin-Mott model [12,15,16] for insulator samples have been employed separately, giving only a partial explanation. To overcome these deficiencies, a reliable and comprehensive model to describe the $\sigma_{THz}(\omega)$ behavior corresponding to the coexistence regime is required.

3.2 Purpose

The purpose of this research is to investigate the electrical transport properties of a phase-separated bulk (La,Pr,Ca)MnO_3 by using the THz-TDS. To do that, I successfully obtained the frequency-dependent THz conductivity at different temperatures ($\sigma_{THz}(\omega,T)$ curves) for (La,Pr,Ca)MnO_3 film. Then I established an insulator-metal composite model by incorporating the Austin-Mott model and the Drude model. This model successfully described the temperature dependence of $\sigma_{THz}(\omega,T)$ curves corresponding to the change in the electronic phase through the IMT. This model enables to concurrently estimate $\sigma_0(T)$ and $X(T)$ at all temperatures. I will explain more detail in the next part.

3.3 Results

3.3.1 Sample preparation and crystal quality

A 350-nm-thick $(La_{0.275}Pr_{0.35}Ca_{0.375})MnO_3$ (LPCMO) epitaxial film on a MgO(001) substrate (LPCMO/MgO) was fabricated by pulsed laser deposition (ArF excimer, λ = 193 nm) under an oxygen pressure of 1 Pa at 1070 K. To improve the film's crystallinity and oxygen stoichiometry, a postannealing process was carried out at 1270 K for 10 h under an oxygen flow. The crystal quality of this LPCMO/MgO film was confirmed by an X-ray diffraction (XRD) measurement (shown in Fig. 3.1). Here the LPCMO(001) single crystal was oriented in the MgO(001) substrate. This film sample was used for the next THz-TDS measurement.

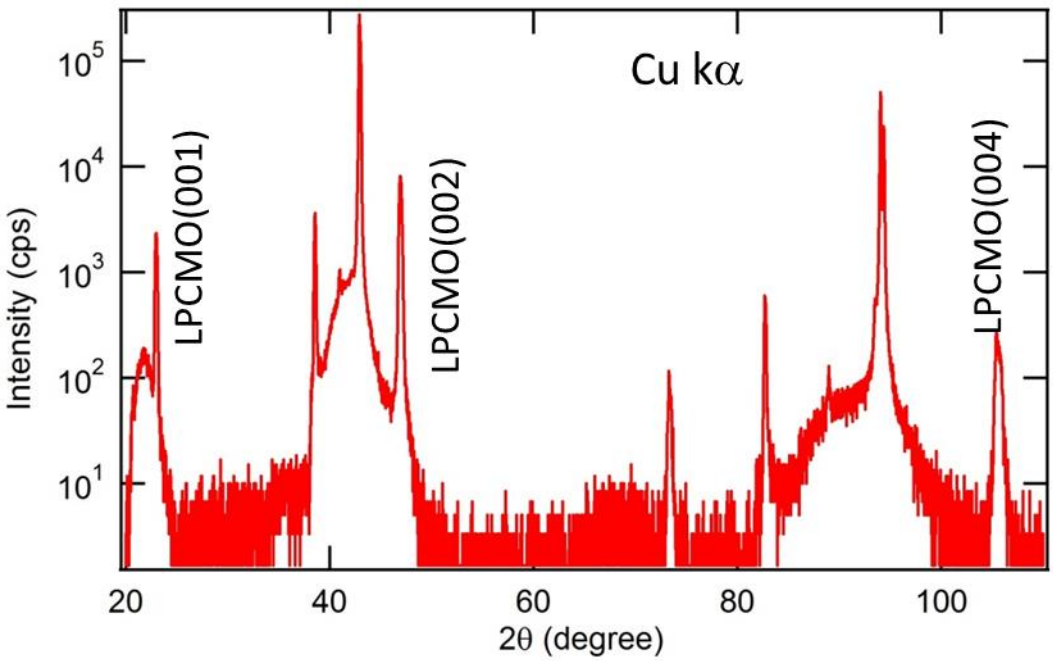

Fig. 3.1: The XRD curve for the LPCMO/MgO film.

3.3.2 THz-TDS measurement

I conducted the THz-TDS measurement for the fabricated LPCMO/MgO sample. Here, the MgO(001) substrate is suitable for THz-TDS because its dielectric constant is independent of the temperature and THz frequency [13]. In the THz-TDS, I measured the transmittance amplitude and the phase in the frequency range from 0.5 THz to 3.4 THz and in the temperature range from 10 K to 250 K. The sample's temperature was constant within ± 0.1 K in each measurement, which was controlled by placing the sample in a helium gas flow-type cryostat. The measurements were performed in dry nitrogen to reduce the absorption peaks from H_2O molecules. The obtained THz pulse passing through the sample is measured in the transmission configuration.

3.3.2.1 The transmitted THz waveforms

Generally the incident THz pulse can be expressed as a propagation, obtained from Maxwell's equations [19-20], whose the electric field propagates along *z* axis and is linearly polarized along *x* axis is:

$$E(r,t) = \frac{1}{2} a(z,t) F(x,y)\, \mathrm{e}^{i(k_0 z - w_0 t)} \qquad (3.1)$$

here $a(z,t)$ is the temporal envelope, $F(x,y)$ is spatial envelope of the pulse (or wave packet); $\nu_0 = {}^{\omega_0}/_{2\pi}$ is the frequency and $k_0 = {}^{\omega_0 n_{(\omega_0)}}/_{c}$ determines the wavelength ($\lambda_0 = {}^{2\pi}/_{k_0}$) of the pulse.

This pulse, after passing through the sample will show the change in the amplitude and the phase. In the THz-TDS, both of these changes in time domain can be detected in the waveforms.

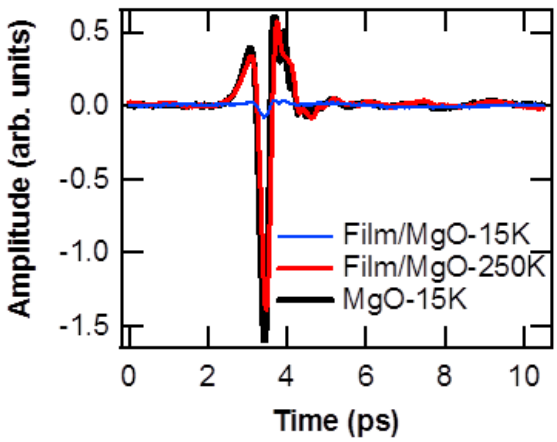

Fig. 3.2: Measured transmitted THz pulses of the LPCMO film on the MgO(001) substrate at 15 K (blue) and 250 K (red) in comparison with that of the bare MgO substrate at 15 K (black).

In the THz-TDS the THz waveform after passing through the LPCMO/MgO sample was measured. To obtain the THz response of the LPCMO film, the contribution of MgO(001) substrate was subtracted. Therefore, the THz waveform passing through MgO(001) substrate was also measured. Figure 3.2 presents typical THz waveforms for the LPCMO/MgO film in the picosecond time domain at 250 K and 15 K (in the cooling process) in comparison with that for the bare MgO(001) substrate at 15 K. The waveform of the film at 15 K showed a typical metallic behavior with strong absorption, i.e., a small value for the amplitude of the transmitted THz wave, while an insulator behavior with high transmittance was observed at 250 K.

These waveforms were transformed to the frequency domain using a fast Fourier transformation (FFT) to obtain power spectra (show the change of amplitude) and phase spectra (show the phase shift) in frequency domain. Fig. 3.3 shows the power spectra and phase spectra of the waveforms in Fig. 3.2.

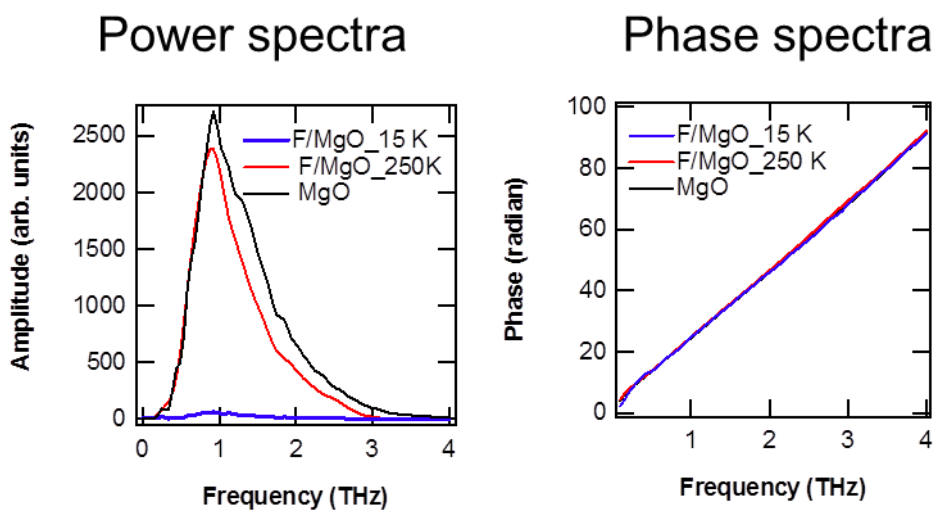

Fig. 3.3: Power spectra and Phase spectra obtained by using FFT of the waveforms of typical F/MgO (at 15 K and 250 K) and MgO samples.

From these spectra, the THz conductivity curve was calculated by using one medium approximation as explained in next part.

3.3.2.2 One medium approximation

In my study, one medium approximation was employed to obtain the THz conductivity of the mix-phase manganite.

General TDS geometry of a thin film deposited on a MgO substrate is illustrated in Fig. 3.4 (lower image) in comparison with that for the measurement of the only MgO substrate (upper image). Here the multiple reflections inside MgO substrate are ignored. The reflective coefficients at interfaces between film - air (r_1) and film - substrate (r_2) are taken into account together with the transmission coefficients.

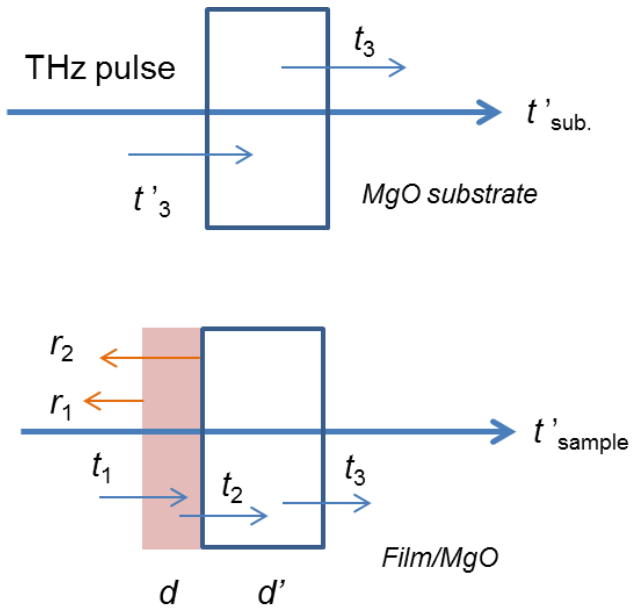

Fig. 3.4: Schematic illustration of the TDS geometry for a MgO substrate (upper image) and a film/MgO substrate (lower image). Arrows represents the direction of the THz beam.

The complex transmission coefficient of MgO substrate is expressed in this equation:

$$t'_{\text{sub.}} = t_3 t'_3 \exp[-i(k_2 - k_0)d'] \tag{3.2}$$

in which d' is the thickness of MgO substrate; $t_3 = \frac{2N_2}{1+N_2}$ is the transmission coefficient from MgO to air; $t_3{}' = \frac{2}{1+2N_2}$ is the transmission coefficient from air to MgO; k_2 is the wave number of MgO, k_0 is the vacuum wave number, N_2 is the complex refractive index of MgO substrate.

The transmission coefficient of the film on MgO substrate (Film/MgO) is:

$$t'_{\text{sample}} = t_1 t_2 t_3 \frac{\exp\{-i[k_1 d + k_2 d' - k_0(d+d')]\}}{1 + r_1 r_2 \exp(-i2k_1 d)} \tag{3.3}$$

here $t_1 = \frac{2}{1+N_1}$ is the transmission coefficient from air to film; $t_2 = 2\frac{N_1}{N_1+N_2}$ is the transmission coefficient from film to MgO, $r_1 = \frac{1-N_1}{1+N_1}$ is the reflective coefficient from the interface between air and film, $r_2 = \frac{N_1 - N_2}{N_1+N_2}$ is the reflective coefficient from the interface between film and MgO substrate; d is the thickness of the film, k_1 is the wave number of the film, $N_1 = \eta_1 + i\kappa_1$ is the complex refractive index of film.

The subtracting the MgO substrate's contribution to the obtained THz pulse passing through the film is conducted as:

$$\frac{t'_{\text{sample}}}{t'_{\text{sub.}}} = \frac{t_1 t_2}{t'_3} \frac{\exp\{-i(k_1 - k_0)\mathrm{d}\}}{1 + r_1 r_2 \exp(-i2k_1 d)} = \frac{A}{A'} \exp[i(\theta - \theta')] \tag{3.4}$$

where A and A' are the amplitudes of the transmissions of Film/MgO, and MgO respectively; θ and θ' are the phase shifts of the transmission of Film/MgO, and MgO

respectively; These parameters can be obtained from the power spectra and phase spectra illustrated in Fig. 3.3. Based on these results, the complex refractive index of the film can be obtained and the real part of the complex THz conductivity also is obtained using the formula from Maxwell's equations:

$$\sigma_{\mathrm{THz}} = \varepsilon_0 \varepsilon_2 \tag{3.5}$$

here ε_0 is the vacuum permissibility, $\varepsilon_2 = 2\eta_1\kappa_1$ is the imaginary part of the complex dielectric constant of film; η_1, κ_1 is the real part and imaginary part of the complex refractive index N_1 of the film.

3.3.2.3 The temperature dependent THz conductivity ($\sigma_{\mathrm{THz}}(\omega,T)$ curves)

The THz conductivity at different temperatures ($\sigma_{\mathrm{THz}}(\omega,T)$ curves) can be obtained from the THz waveform passing through the sample using equations (3.4) and (3.5) as explained in the section 3.3.2.2

Figure 3.5 displays the frequency dependence of the THz conductivity at different temperatures ($\sigma_{\mathrm{THz}}(\omega,T)$ curves) during the cooling process.

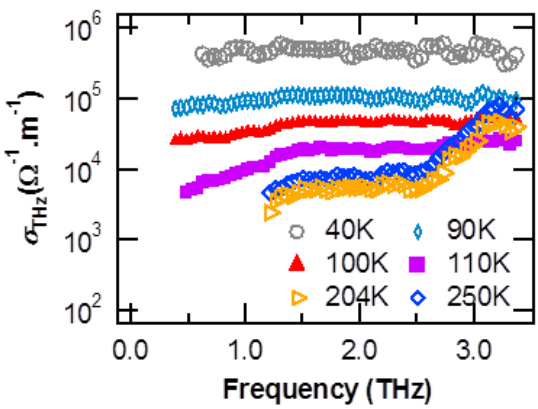

Fig. 3.5: Frequency dependence of the THz conductivity for the 350-nm-thick LPCMO film at different temperatures.

It can be clearly seen that below 2.5 THz, the conductivity increased with decreasing temperature, which revealed the IMT process in the sample. Above 2.5 THz, a phonon peak at ~ 3.2 THz (equal to 107.3 cm^{-1}) [18] was observed at high temperatures (above 120 K). Moreover, in the frequency region from 0.5 THz to 2.5 THz, the $\sigma_{THz}(\omega,T)$ curves showed that as frequency increased, the conductivity at 40 K was almost constant, while that at 250 K increased, and interestingly, the conductivity at intermediate temperature, for example at 110 K, showed the complicated tendency with both increasing and constant behaviors. These results suggested a mixed-state in the sample at intermediate temperatures. To thoroughly explain the temperature-induced change of $\sigma_{THz}(\omega,T)$ curves in the frequency range from 0.5 THz to 2.5 THz, a comprehensive model should be proposed which can fulfill the lack of the convention model. This will be introduced in the next part.

3.4 Discussion

3.4.1 The Insulator-metal composite model

In this part I will introduce the original idea and theoretical background to construct a model to explain $\sigma_{THz}(\omega,T)$ curves in the phase-separated material.

3.4.1.1 THz conductivity for the mixed-phase material

In my study, the THz-TDS was conducted for a mix-phase material with two different states: Insulator and Metal. In order to employ one medium approximation, I proposed that two phases are arranged as illustrated in Fig. 3.6. As a result, the total observed THz conductivity is the summation of the conductivities of insulator

component σ^{I} and metal component σ^{M} with the corresponding ratio, as expressed in this equation:

$$\sigma_{\mathrm{THz}}\mathrm{observed} = (1 - X(T))\sigma^{\mathrm{I}}\ (T) + \ X\sigma^{\mathrm{M}}(T) \tag{3.7}$$

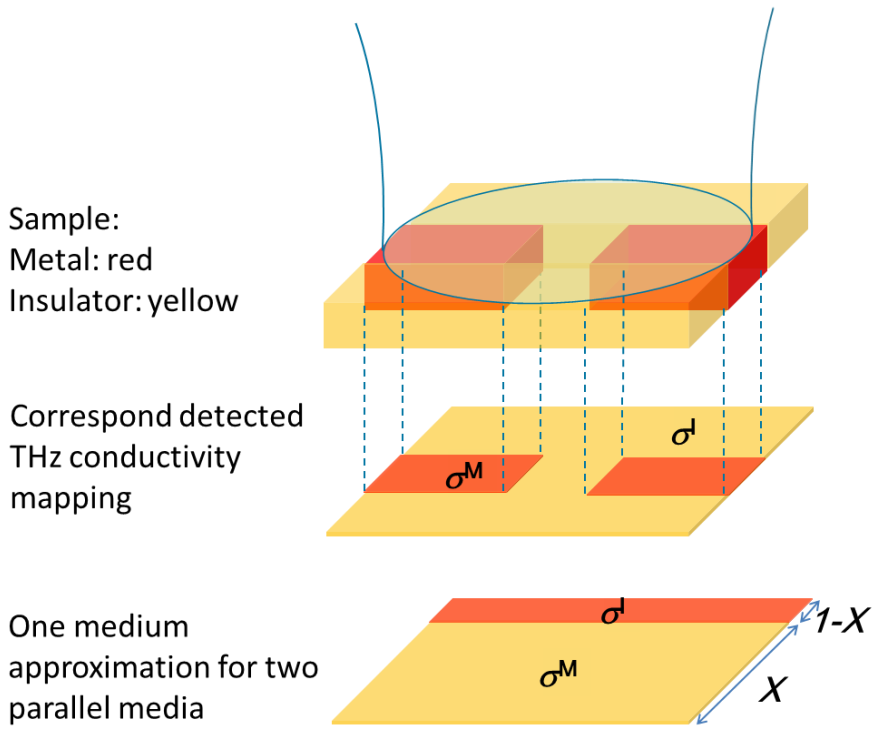

Fig. 3.6: Schematic illustration of the one medium approximation for a mix-phase manganite.

It is well-known that the ac conductivity for metal component is characterized by the Drude model. For the insulator component, it follows the Austin-Mott model. In the next part, I will introduce these models and explain how I can construct my composite model.

3.4.1.2 Drude model for metal

To understand the optical response of a metal, in 1900 Drude treated a metal as a free-electron gas to conduct a diffusive motion. Upon the application of a field: $\mathbf{E}(t) = \mathbf{E}_0 exp(-i\omega t)$, the equation of motion for free electron in metal is:

$$m\frac{d^2\boldsymbol{r}}{dt^2} + \frac{m}{\tau}\frac{d\boldsymbol{r}}{dt} = -e\boldsymbol{E}(t) \tag{3.8}$$

where m is the electron mass; e is the magnitude of electronic charge. The second term in this equation represents the viscous damping and related to an energy loss mechanism with the corresponding relaxation time τ.

The solution of this equation gives a frequency dependent complex conductivity:

$$\sigma(\omega) = \sigma_1(\omega) + i\sigma_2(\omega) = \frac{Ne^2\tau}{m}\frac{1}{1-i\omega\tau} = \frac{Ne^2\tau}{m}\frac{1+i\omega\tau}{1+\omega^2\tau^2} = \frac{\omega_p^2}{4\pi}\frac{1}{1/\tau - i\omega} \tag{3.9}$$

in which $\omega_p$is the plasma frequency

In my study, the THz frequency range is from ω ~ 1 – 2.5 THz and the typical value of τ for a metal is 0.05s ($1/\tau$ ~ 15 THz), thus: ω ≪ $1/\tau$ and $\sigma_{ac} \approx \sigma_1(\omega) \gg \sigma_2(\omega)$ and therefore $\sigma_1(\omega)$ is frequency independent for a typical metal.

3.4.1.3 Austin-Mott model for insulator

Hopping conduction of carriers in insulators was predicted quite a long time ago since the prediction on the electron hopping between localized states of Gudden and Schottky in 1935. A lot of experimental works [11,12,15,16] were conducted to confirm the increase of ac conductivity with the increase of frequency as a result of the hopping's encouragement, for example the study of Austin and Mott in 1969.

More general, the ac conductivity is related to the dc conductivity and frequency following this equation:

$$\sigma(\omega) \sim \sigma_{dc} + A\omega^{s} \tag{3.10}$$

where A is hopping amplitude and s is a power parameter. Following Austin-Mott formula[15] the value of A is related to the density of states at the Fermi level.

The common mechanism for this feature was the charge carriers involved move by discontinuous hopping movements between localized sites and they may be electrons, polarons or various ions.

3.4.1.4 Insulator-metal composite model

Since the coexistence of the metal and insulator phases in the mixed-phase manganite at intermediate temperatures was observed in the THz conductivity curves shown in section 3.3.2.3, I proposed a composite model to describe the $\sigma_{\mathrm{THz}}(\omega,T)$ curves, typically in the frequency range below 2.5 THz which is a combination of the Austin-Mott model and the Drude model with their corresponding contribution $X(T)$:

$$\sigma_{\mathrm{THz}}(\omega, \mathrm{T}) = (1 - X(T))(\sigma_0^{\mathrm{I}}(T) + A\omega^{s}) + \mathrm{X}(T)\frac{\sigma_0^{\mathrm{M}}(T)}{1+\tau^2\omega^2}. \tag{3.11}$$

Here, $\sigma_0^{\mathrm{I}}(T)$ and $\sigma_0^{\mathrm{M}}(T)$ are the THz conductivity at a frequency of 0 THz (or the dc conductivity for insulator and metal domains, respectively; $X(T)$ is defined as the fraction of the metal phase in the system at temperature T. Using the composite model, I have least-square fitted $\sigma_{\mathrm{THz}}(\omega,T)$ curves at all temperatures. The typical fitting results are shown in Fig. 3.7.

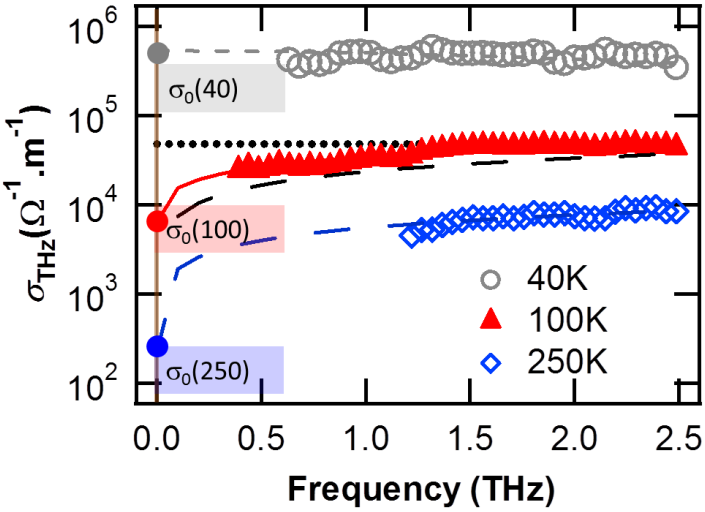

Fig. 3.7: $\sigma_{\mathrm{THz}}(\omega,T)$ curves at 40 K (gray circles), 100 K (red triangles), and 250 K (blue lozenges). Typical fitted curves with eq. (1) are presented: the gray dotted curve at 40 K where X = 1; the solid red curve at 100 K where X = 0.68; and the blue dash-dot curve at 250 K where X = 0.

For example, at 250 K, the $\sigma_{\mathrm{THz}}(\omega,T$=250 K) curve exhibited a characteristic power law feature following the Austin-Mott model [15], in which the conduction of strongly localized carriers occurs between two randomly distributed centers: $\sigma_{\mathrm{THz}}(\omega,T) = \sigma_0^{\mathrm{I}}(T) + A\omega^s$[11,12,16]. Here, the value of s was fixed at 0.5 for all temperatures, which is a characteristic of a system with strong electron – electron interactions [16,19]. The blue dash curve in Fig. 3.7 showed the well-fitted result with eq. (3.11) where X was close to 0, in comparison with the experimental data (blue lozenges). At 40 K, the $\sigma_{\mathrm{THz}}(\omega,T$=40 K) curve exhibited Drude-like metallic behavior: $\sigma_{\mathrm{THz}}(\omega,T) = \frac{\sigma_0^{\mathrm{M}}(T)}{1+\tau^2\omega^2}$ [8,10]. The gray dash curve in Fig. 3.7 displays a typical fit result with eq. (3.11) where X was about, in comparison with the experimental data (gray circles).

The representative fit result with eq. (1) for the $\sigma_{THz}(\omega,T)$ curve at 100 K (solid red curve) is shown in Fig. 3.7, where X was about 0.69. If only the Austin-Mott part (X=0) or the Drude part (X=1) in eq. (1) had been employed for fitting, significant deviations between the fitted curves (shown as black dashes and black dots, respectively) and the experimental data would have been observed. This implies that the composite model is much more suitable for explaining the conductivity at all temperatures, particularly in the coexistence region. The relaxation time τ in eq. (3.11) obtained by fitting showed a weak dependence on the temperature [12,19]. τ was about 60 fs, which is typical for the free electrons in a metal [20].

3.4.2 Electrical transport properties

Based on the fitting parameters, I obtained the temperature dependence of the metal fraction $X(T)$ in the cooling process as presented in Fig. 3.8.

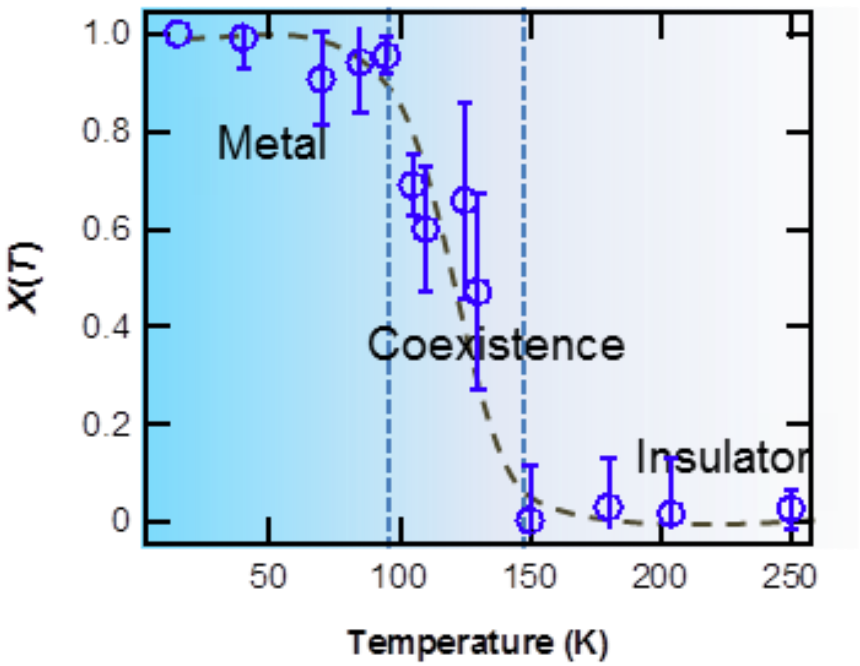

Fig. 3.8: Evolution of metal fraction $X(T)$ during the cooling process. The dashed line between the points is a guide for the eyes.

In this figure, it can be seen that, above 150 K, X was approximately 0, then X increased with decreasing temperature and became about 1 below 100 K. This result reveals the phase condition, namely, the pure insulator phase at high temperatures, the coexistence of metal and insulator phases at intermediate temperatures, and the metal phase at low temperatures. Moreover, this result shows the quantitative variation of the metal and insulator phases associated with the IMT process in this system. So far, the fraction of metal phase in the coexistence region has been estimated by observation, typically using scanning probe microscopy and transmission electron microscopy [1,2]. Compared with these microscopy techniques, our method based on THz-TDS has the advantage of enabling quantitative investigation of the metal fraction in addition to the simultaneous estimation of the conductivity.

Also, the THz conductivity in the vicinity of 0 THz, $\sigma_0(T)$, was numerically estimated by extrapolating the $\sigma_{\mathrm{THz}}(\omega,T)$ curves to 0 THz using eq. (1). The temperature dependence of $\sigma_0(T)$ result for the cooling process (red dots) is displayed in Fig. 3.9. In this figure, it can be seen that the obtained $\sigma_0(T)$ changed by about five orders of magnitude through the T_c, approximately 150 K during the cooling process.

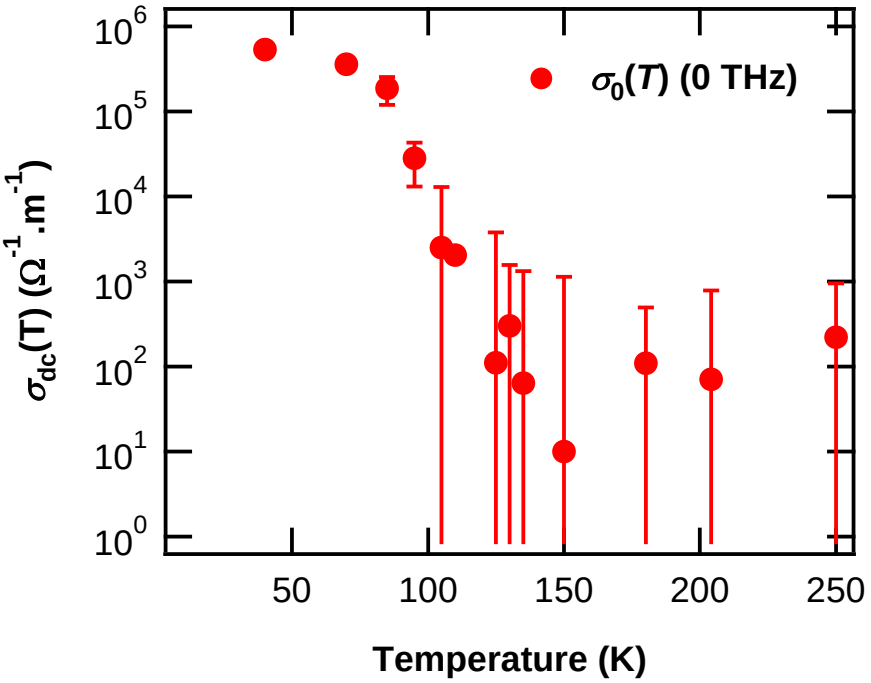

Fig. 3.9: Estimated values of $\sigma_0(T)$ for the cooling (red dots).

I also measured the dc electrical conductivity using 4-probe measurement. Figure 3.10 exhibits the dc electrical conductivity curve $\sigma_{dc}(T)$ for the LPCMO/MgO film during cooling (blue circles) and heating (red triangles) processes. The rapid change in conductivity during the cooling process indicates the phase transition from the insulator phase at high temperatures to the metal phase at low temperatures and vice versa during the heating process.

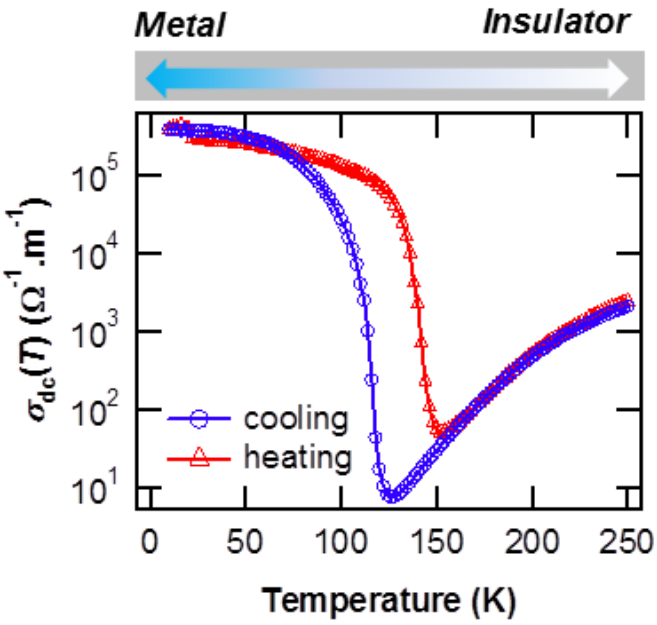

Fig. 3.10: Temperature dependence of the dc conductivity of a LPCMO film on a MgO(001) substrate during cooling (blue circles) and heating (red triangles) processes (4-probe electric measurement).

Then the comparison between estimated the dc conductivity $\sigma_0(T)$ at 0 THz and measured dc conductivity $\sigma_{dc}(T)$ by 4-probe electric measurement (blue line) is shown in Fig. 3.11 (in the cooling process). It can be seen that the $\sigma_0(T)$ curve closely agreed with the $\sigma_{dc}(T)$ (4-probe) curve. These results illustrate the potential of my insulator-metal composite model for investigating the dc conductivity using THz-TDS. By combining the Drude and Austin-Mott models, I succeeded in improving the conventional analysis methods, which showed the rather poor agreement between the model and experimental values for the phase-separted systems. Since our model is in agreement with the phase-separated scenario for mixed-phase materials, the present analysis also enables me to obtain the fraction of metal phase through the transition as shown in Fig. 3.8.

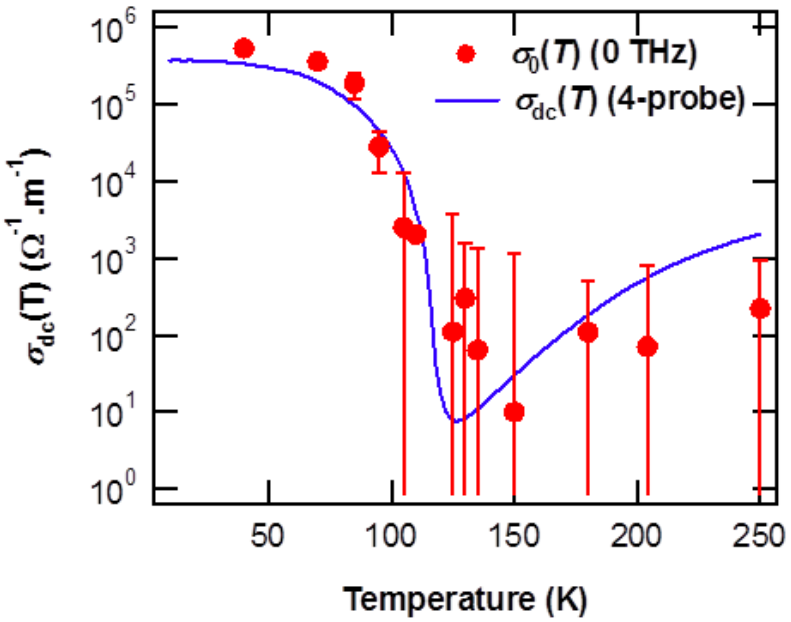

Fig. 3.11: Estimated values of $\sigma_0(T)$ for the cooling (red dots) in comparison with the dc conductivity measured by 4-probe electric measurement (blue line).

Conventional electrical measurement can generally be applied to demonstrate the transport dynamics in a material with the conduction of free electrons by probing the behavior of electrons near the Fermi level. Because of the power-law rise in conductivity with increasing frequency, the conductivity in the insulator phase is more easily and accurately detected at higher frequencies. The composite model for describing the frequency-dependent THz conductivity can reveal the change in the electron conductivity behavior from the hopping of strongly localized electrons to their free movement, corresponding to the IMT of LPCMO. Thus, our model is more effective for investigating the transport properties of electrons than conventional electrical measurement.

3.5 Conclusion

In summary, I have realized a model for analyzing the THz conductivity $\sigma_{\mathrm{THz}}(\omega,T)$ of a strongly correlated LPCMO film by incorporating Austin-Mott and Drude models. In my study, this model enables the simultaneous estimation of $\sigma_0(T)$, which is equivalent to the dc electrical conductivity, and $X(T)$ which indicates the domain dynamics, i.e., the population of metal and insulator domains, in IMT/MIT processes. Additionally, the estimated microscopic conductivities at 0 THz for the metal ($\sigma_0^{\mathrm{M}}(T)$) and insulator domains ($\sigma_0^{\mathrm{I}}(T)$), together with their contribution $X(T)$ to the total conductivity, provide the possibility of unveiling the complex properties of phase-separated materials. A further advantage of the present model applied in the THz-TDS results is its contact-free manner which can be applied to various samples with any shape and size. In particularly, for nanoscale phase-separated samples, in which the contribution of each domain to the conductive property is accelerated, our established model is expected to be more effective than the use of a probe, and may eventually lead to the tuning of domain dynamics.

3.6 References

1. L. Zhang, C. Israel, A. Biswas, R. L. Greene, A. de Lozanne, Science **298** (2002) 805
2. M. Fäth, S. Freisem, A. A. Menovsky, Y. Tomioka, J. Aarts, J. A. Mydosh, Science **285** (2005) 1540
3. M. M. Qazilbash, M. Brehm, B.-G. Chae, P.-C. Ho, G. O. Andreev, B.-J. Kim, S. J. Yun, A. V. Balatsky, M. B. Maple, F. Keilmann, H.-T. Kim, D. N. Basov, Science **318** (2007) 1750
4. M. Uehara, S. Mori, C. H. Chen, and S.-W, Cheong, Nature **399** (1999) 560
5. T. V. A. Nguyen, A. N. Hattori, Y. Fujiwara, S. Ueda, H. Tanaka, Appl. Phys. Lett. **103** (2013) 223105
6. Y. Yanagisawa, H. Tanaka, T. Kawai, L. Pellegrino, Appl. Phys. Lett. **89** (2006) 253121
7. K. R. Mavani, M. Nagai, D. S. Rana, H. Yada, I. Kawayama, M. Tonouchi, K. Tanaka, Appl. Phys. Lett. **93** (2008) 231908
8. R. Rana, P. Pandey, D. S. Rana, K. R. Mavani, I. Kawayama, H. Murakami, M. Tonouchi, Phys. Rev. B **87** (2013) 224421
9. T. Ohba, S. Ikawa, J. Appl. Phys. **64** (1988) 4141
10. N. Kida, M. Hangyo, M. Tonouchi, Phys. Rev. B **62** (2000) R11965
11. P. Lunkenheimer, A. Loidl, Phys. Rev. B **91** (2003) 207601
12. A. Pimenov, S. Tachos, T. Rudolf, A. Loidl, D. Schrupp, M. Sing, R. Claessen, V. A. M. Brabers, Phys. Rev. B **72** (2005) 035131
13. D. Grischkowsky, S. Keiding, Appl. Phys. Lett. **57** (1990) 1055

14. J. R. Simpson, H. D. Drew, V. N. Smolyaninova, R. L. Greene, M. C. Robson, A. Biswas, M. Rajeswari, Phy. Rev. B **60** (1999) R16263
15. I. G. Austin, N. F. Mott, Adv. Phys. **18** (1969) 41
16. Y. Akishige, T. Fukatsu, M. Kobayashi, E. Sawaguchi, Jour. Phys. Soc. Jpn. **54** (1985) 2323
17. H. Shimosato, T. Katashima, S. Saito, M. Ashida, T. Itoh, K. Sakai, Phys. Stat. Sol. (c) **3** (2006) 3484
18. V. B. Podobedov, A. Weber, D. B. Romero, J. P. Rice, H. D. Drew, Phys. Rev. B **58** (1998) 43
19. M. Dressel, G. Grüner, *Electrodynamics of Solids*, Cambridge University Press, Cambridge (2002) p.329
20. F. Wooten, *Optical Properties of Solids*, Academic Press, New York and London (1972) p.53

CHAPTER 4

Electrical transport properties in phase-separated $(La,Pr,Ca)MnO_3$ nanowires investigated by terahertz time domain spectroscopy

Abstract

I investigated the electrical transport properties, i.e., domain evolution $X(T)$ and dc conductivity $\sigma_{dc}(T)$ in a typical (La,Pr,Ca)MnO_3 nanowires sample through the metal-insulator transition using terahertz time domain spectroscopy. By choosing a parallel configuration between the wire alignment versus the polarization of THz pulse, I could obtain the intrinsic temperature-induced conductivity behavior change in a nanowires sample with 100-nm-width and 60-nnm-height which followed the transition from metallic to insulating behavior as temperature increased. The $X(T)$ and $\sigma_{dc}(T)$ were estimated by fitting THz conductivity curves with an insulator-metal composite model.

4.1 Introduction

The transition metal oxides with strongly correlated electrons have emerged as new types of materials with variety of functionalities such as the colossal magnetoresistivity in manganites [1-2], or the high-T_C superconductivity in cuprates [3]. Of particular interest is a typical perovskite manganite (La,Pr,Ca)MnO_3 which exhibits the metal - insulator transition (MIT) from a metallic behavior at a low temperature to an insulator behavior at a high temperature [4]. At intermediate temperatures, the so-called coexistence region has been reported in which both metal and insulator domains exist in the nanometer scale [5]. These electronic domains with their own conductivity associated with effective carriers contribute independently to the total observed MIT behavior [6]. Interestingly, peculiar operations were observed in the nanometer scale phase-separated materials in which the electric domains were

confined [7-9]. For example the digitalized magnetoresistance has been reported in the (La,Pr,Ca)MnO_3 nanochannel structures [8]. To understand their nanopeculiar conductive property, the quantitatively estimation of domain evolution, i.e., the temperature-induced change of the metallic phase $X(T)$ becomes extremely important. Moreover, the investigation of electrical transport properties which shows the correlation between the domain evolution $X(T)$ and conductivity behavior $\sigma_{dc}(T)$ is not only of fundamental interest in elucidating the MIT behavior, but also of practical meaning in realizing new functionalities for oxides electronics devices.

So far, the spatial distribution of domains in phase-separated nanostructures could be observed in VO_2 nanobeams using a microscope technique [10], or the domain revolution $X(T)$ could be inferred in (La,Pr,Ca)MnO_3 nanoboxes using hard X ray photoemission spectroscopy [4]. However the extremely strict requirements for those measurements and the lack of observable physical parameters such as dc conductivity usually hamper the wide applicability of those techniques. On the other hand, the dc electrical transport measurement using attached electrodes was widely employed to measure $\sigma_{dc}(T)$, but the $X(T)$ was hard to be evaluated. In the chapter 3, the technique for simultaneous evaluation of $X(T)$ and $\sigma_{dc}(T)$ for a 300-nm-effective thickness (La,Pr,Ca)MnO_3 film has been established by using terahertz time domain spectroscopy (THz-TDS) [6]. In this manner, a waveform passing through a phase-separated material was used to estimate its THz conductivity at different temperatures ($\sigma_{THz}(\omega,T)$ curves). Then the insulator-metal composite model was proposed to explain the behavior of $\sigma_{THz}(\omega,T)$:

$$\sigma_{\mathrm{THz}}(\omega,\mathrm{T}) = (1 - X(T))(\sigma_0^{\mathrm{I}}(T) + A\omega^s) + \mathrm{X}(T)\frac{\sigma_0^{\mathrm{M}}(T)}{1+\tau^2\omega^2}. \quad (4.1)$$

The first term in Eq. (1) characterizes the hopping of localized electrons which follows the Austin-Mott model. A and s are the amplitude and power parameter of the hopping process [11-13]. The second term in Eq. (1) explains the conductivity behavior of free electrons with a relaxation time τ according to the Drude model [14,15]. Here, $X(T)$ is defined as the fraction of metallic phase in the system at a temperature T, $\sigma_0^{\mathrm{I}}(T)$ and $\sigma_0^{\mathrm{M}}(T)$ are the THz conductivities at 0 THz for insulator and metal phases, respectively. This model enabled the investigation of the correlation between $X(T)$ and $\sigma_{\mathrm{dc}}(T)$.

For phase-separated nanostructures, such as nanowires, this technique is promising to investigate their intrinsic electrical transport properties in a non-contact manner as shown in figure 4.1.

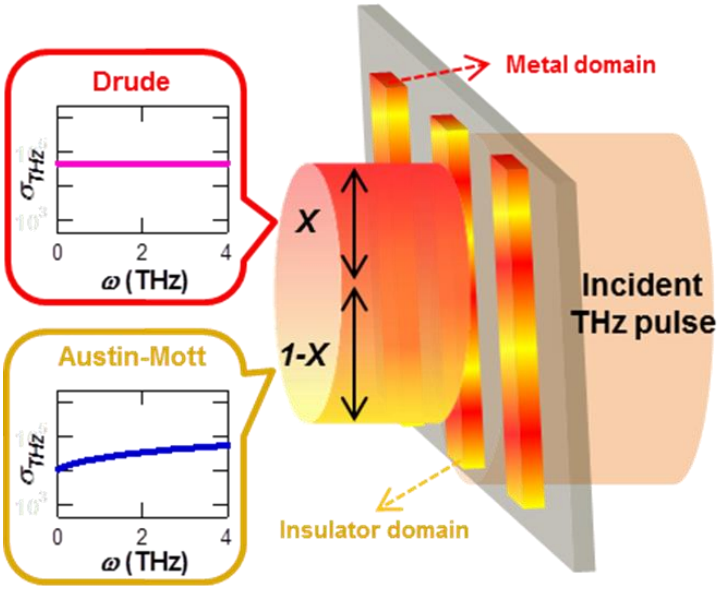

Fig. 4.1: Schematic illustration for investigation of transport dynamics in a phase-separated nanowires structure.

By the way, to apply this method for a nanowires structure, all external effects should be considered. An example of external effect is the structure effect which relates to the wire alignment versus the polarization of incident THz pulse $\vec{P}$. So far,

the structure effect, observed in a millimeter-scale phosphor bronze wire grids sample, showed the change in frequency dependent behavior of dielectric constant with different wire alignments [11]. This effect might appear in nanowires samples and should be excluded to obtain their intrinsic electrical transport properties originating from the phase-separated domains. Also, one of the approaching ways to obtain enough signal-noise ratio in a THz-TDS set-up is to fabricate the sample with the size, at least equals to the beam size of about 3 mm^2 and the required effective thickness of about few ten nanometers. These demands become challenging points for the measurements of nanowires samples due to their small volume.

4.2 Purpose

In this research, I will show an efficient route to investigate the transport dynamics in a $(La,Pr,Ca)MnO_3$ nanowires sample which was fabricated with a high density over a large area. Then the structure effect in a typical nanowires sample will be presented. After excluding the structure effect, I could obtain its intrinsic electrical transport properties by analyzing the THz conductivity behavior with the insulator-metal composite model [6]. The next part will exhibit these results.

4.3 Experiment

The high density $(La_{0.275}Pr_{0.35}Ca_{0.375})MnO_3$ (LPCMO) nanowires sample was fabricated on a MgO(001) substrate by a nanoimprint lithography (NIL) - based procedure. First, a single phase crystallized LPCMO film was deposited on the MgO(001) substrate (LPCMO/MgO) by a pulsed laser deposition technique. The laser (ArF excimer, λ = 193 nm) fluence was 2 J/cm^2 and the deposition was conducted under an oxygen pressure of 30 Pa at 973 K. To improve the film's crystallinity and

oxygen stoichiometry, an in-situ post-annealing process was carried out at 973 K for 1 hour under an oxygen flow of 1000 Pa. Then a high density resist nanowires pattern (line space ratio of 1:3) was prepared on the surface of the LPCMO/MgO film by the NIL technique over a large area of more than 3 mm^2. The LPCMO nanowires sample was obtained after etching process using electron cyclotron resonance plasma. A post - annealing process at 873 K was conducted under an oxygen flow in 2 hours to compensate the oxygen vacancies appeared in the sample treatment process.

The height and pattern topography of the nanowires sample were evaluated by an atomic force microscope (AFM, NanoNavi E-sweep, Hitachi) and a field-emission scanning electron microscope (SEM, SU-9000, Hitachi), respectively at room temperature. Electrodes used for electrical transport measurements were prepared as an electron-beam-deposited bilayer film of Ni/Au. The dc electrical conductivity was measured by a source-meter unit (2612A, Keithley Instruments). In THz-TDS measurement, I determined the waveforms (transmittance amplitude and phase) of the THz pulse in a frequency range from 0.5 THz to 4.0 THz and in a temperature range from 10 K to 300 K. The sample's temperature was constant within ± 0.1 K in each measurement. The temperature was controlled by placing the sample in a helium gas flow-type cryostat for both electric and THz-TDS measurements. The THz-TDS measurements were performed in dry nitrogen to reduce the absorption peaks from H_2O molecules. In THz region, the nanowires sample behaves as a continuous film as their characteristic scales, such as the width, are much smaller than the THz wavelength, so the homogeneous film approximation has been employed when calculating the conductivity [11].

4.4 Results and Discussion

4.4.1. The LPCMO nanowires structure

Figure 4.2 exhibits a typical SEM image of a LPCMO nanowires sample over a large area with a 100 nm width (inset SEM image in the left) and a 60 nm height (inset AFM image in the right). The line space ratio in this high density LPCMO nanowires sample, exactly transferred from NIL resist pattern, was of 1:3, i.e., the coverage of 25 percent which corresponded to a film with an effective thickness of about 15 nm.

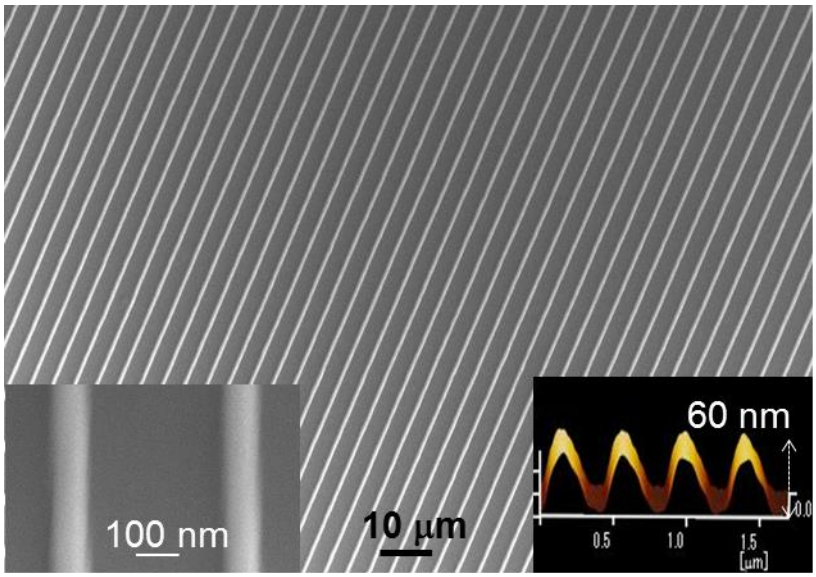

Fig. 4.2: Typical SEM image of high-density LPCMO nanowires with 100-nm-width (inset SEM image in the left) and 60-nm-height (inset AFM image in the right).

The LPCMO nanowires sample had the pseudo-cubic perovskite structure with the (001) orientation on the MgO(001) substrate as confirmed using an X-ray diffraction measurement (Figure 4.3). Therefore by using a NIL - based procedure, I could fabricate the high density LPCMO nanowires on a MgO(001) substrate over a large area of more than 3 mm^2 which can be measured by the THz-TDS.

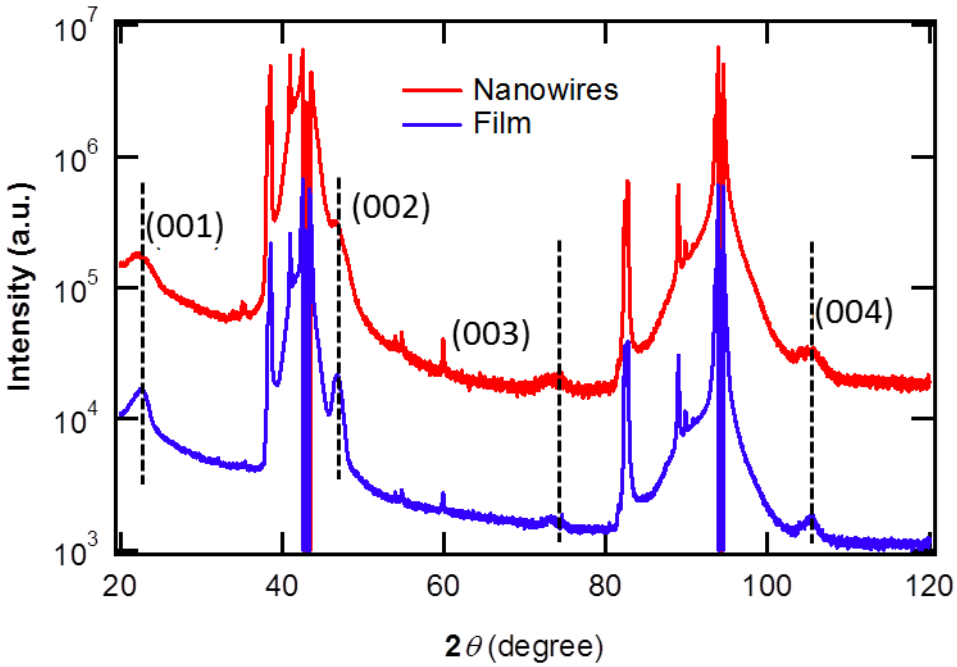

Fig. 4.3: XRD curve of the LPCMO nanowires sample in comparison with the LPCMO film.

4.4.2. The structure effect

To check the structure effect for the LPCMO nanowires sample in THz-TDS, I set the temperature at 10 K so that the sample became metallic. I chose two different configurations for measurement. In the first configuration, called α=0° configuration, the wire alignment was parallel to the polarization $\vec{P}$ of incident THz pulse. In the second set-up, the so-called α=90° configuration, the wire alignment was perpendicular to $\vec{P}$. We could clearly observe the reduction of intensity of transmitted THz pulse in the α=0° configuration compared with that in the α=90° configuration. In figure 4.4, the waveform in α=0° configuration (red) showed a typical metallic behavior with strong absorption, while only a smaller change of waveform's intensity was observed for that sample in α=90° configuration (blue) compared with that of the MgO substrate (black).

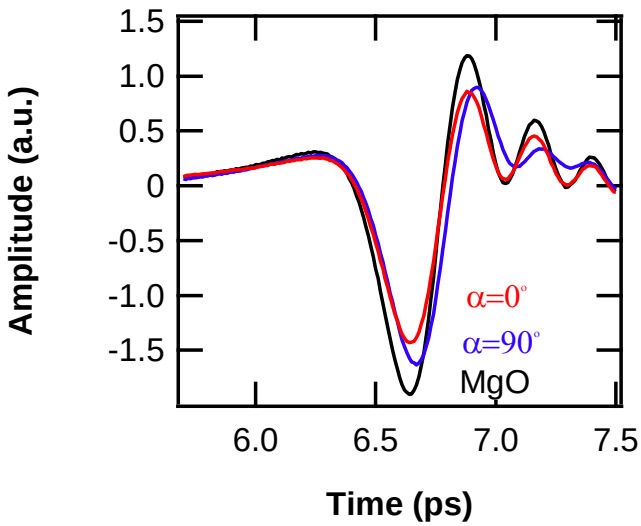

Fig. 4.4: The THz waveforms passing through the LPCMO nanowires/MgO(001) substrate in α=0° configuration (red), and α=90° configuration (blue), compared with that of the bare MgO(001) substrate (black).

These waveforms in a time domain were Fourier transformed to a frequency domain and then numerically analyzed by subtracting the contribution of MgO(001) substrate, to estimate the corresponding THz conductivity ($\sigma_{THz}(\omega)$ curves) as shown in figure 4.5 (a).

It can be seen that in the α=0° configuration, $\sigma_{THz}(\omega)$ curve (red triangles) showed the Drude behavior [14] with a tiny reduction of the conductivity as the frequency increased which confirmed the metallic feature of the LPCMO nanowires sample at 10 K. This behavior could be explained by the conduction of free carriers along the nanowires as $\vec{P}$ was parallel to wires (figure 4.5 (b)). On the other hand, in the α=90° configuration, the dielectric/insulator behavior was observed with the increase of conductivity as the frequency rose which followed the Austin-Mott model [13]. The insulating behavior observed in the α=90° configuration might originate from the capacitance between nanowires which prevented the conduction of carriers

as $\vec{P}$ was perpendicular to the wires. This observed result is similar with the previous research in a phosphor bronze wire grids sample [10]. We also checked the structure effect in a typical LPCMO nanowires sample through the MIT process, from a low temperature (10 K) through an intermediate point (120 K) to a high temperature (280 K). The results showed the decrease of the amplitude of the waveform as temperature increased inferring the MIT process in the α=0° configuration. On the other hand, for the case of α=90° configuration, the waveform's amplitude was always close to that of the MgO substrate at all temperatures, suggesting the interruption of carrier motion, i.e., the scattering effect at the boundary of nanowires.

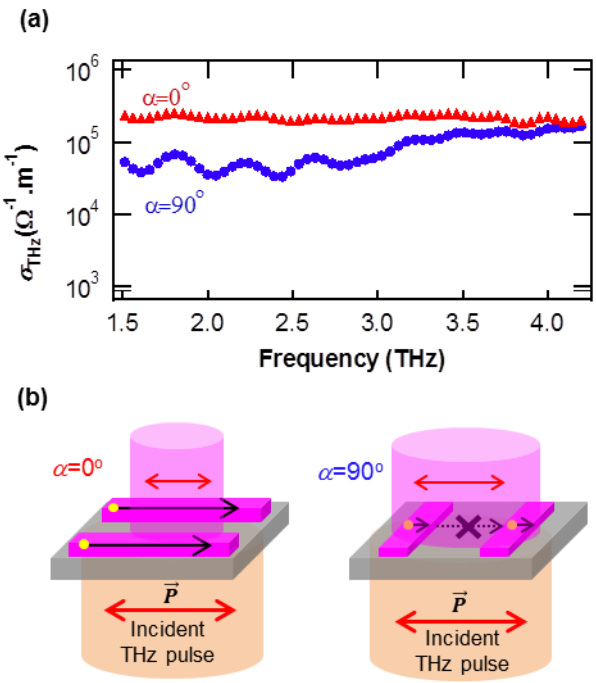

Fig. 4.5: (a) Conductivity curve change from metallic behavior (red triangles) to dielectric behavior (blue dots) due to the structure effect. (b) The schematic illustration of structure effect in a LPCMO nanowires sample in the metallic state with α=0° and α=90° configurations: yellow dots are carriers with their corresponding conduction path.

4.4.3. Electrical transport properties of LPCMO nanowires sample

To obtain intrinsic conductive behavior in the LPCMO nanowires sample, I have employed the α=0° configuration for further temperature dependent THz-TDS measurements. The frequency dependent THz conductivity ($\sigma_{THz}(\omega,T)$ curves) for the LPCMO nanowires sample was measured at different temperatures. The typical results are shown in Fig. 4.6.

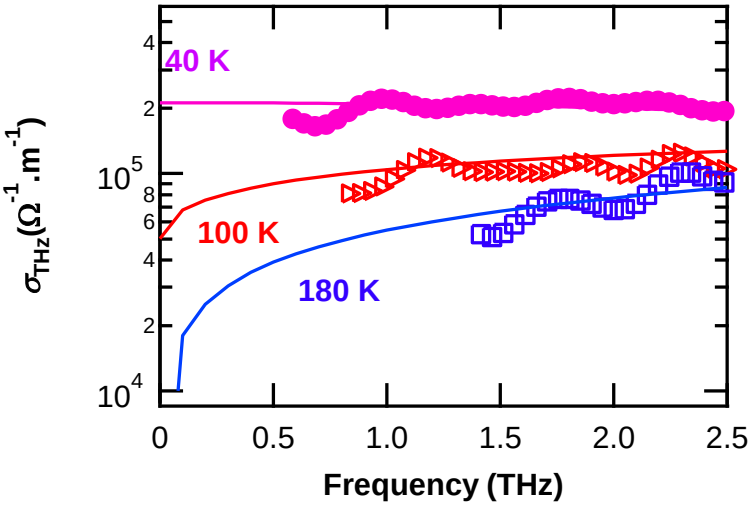

Fig. 4.6 THz conductivity $\sigma_{THz}(\omega,T)$ curves for the LPCMO nanowires sample at three typical temperatures (in α=0° configuration) and their corresponding fit curves (lines).

Figure 4.6 displays the frequency dependence of THz conductivity at three typical temperatures (40 K, 100 K, and 180 K) for the LPCMO nanowires sample during the heating process. It can be clearly seen that the conductivity decreased as the temperature went up, which corresponded to the MIT process in this sample. Also, I could observe the change in $\sigma_{THz}(\omega,T)$ curves' behavior as the temperature varied. For example as the frequency increased, the conductivity at 40 K (magenta dots) was almost constant while that at 180 K (blue squares) obviously raised and that at 100 K

(red triangles) showed the intermediate state. These results were consistent with previous data of the LPMCO film in chapter 3.

Next, I discuss on the investigation of the electrical transport properties for the LPCMO nanowires sample. By least-square fitting the $\sigma_{THz}(\omega,T)$ curves with Eq. (4.1) (corresponding dash curves in Fig. 4.6), I could obtain the corresponding fit parameters such as X, σ_0^I, σ_0^M, A, τ. Here, the power parameter s was fixed at 0.5 for all temperatures, which is the characteristic of a system with strong electron – electron interactions [16,17]. The A and τ values were almost constant and consistent with the typical values for strongly correlated system [15,18]. Remarkably, the temperature dependence of metal fraction $X(T)$ in the heating process was obtained. The result in Fig. 4.7 showed that below 90 K, X was approximately 1, then X suddenly went down to about 0.34 at around 90 K with increasing temperature and became about 0 at temperatures above 150 K.

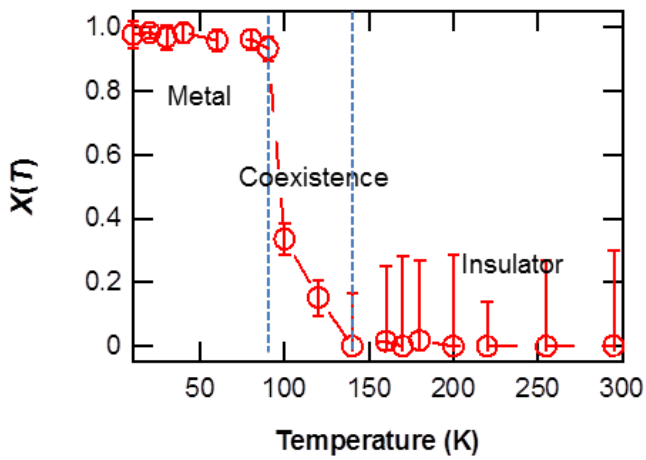

Fig. 4.7: Temperature dependence of metal fraction in a LPCMO nanowires sample. The dashed line between the points is a guide for the eyes.

This result quantitatively presented the change of phase from the pure metal phase at low temperatures to the insulator phase at high temperatures through the

coexistence region at intermediate temperatures. This changing behavior revealed the domain evolution through the transition which is in agreement with the phase-separated scenario for this material.

4.4.4. Nanopeculiar properties of LPCMO nanowires sample

Interestingly, we found the nanopeculiar transition property in the $X(T)$ behavior of the nanowires sample (red squares) in comparison with that of a film (blue dots). In fig. 4.8, it can be seen that the X value in the nanowires sample suddenly reduced at about 90 K, while it gradually changed in the film. This might come from the reduction of the sample's volume, i.e., the decrease of total number of domains in the nanowires sample.

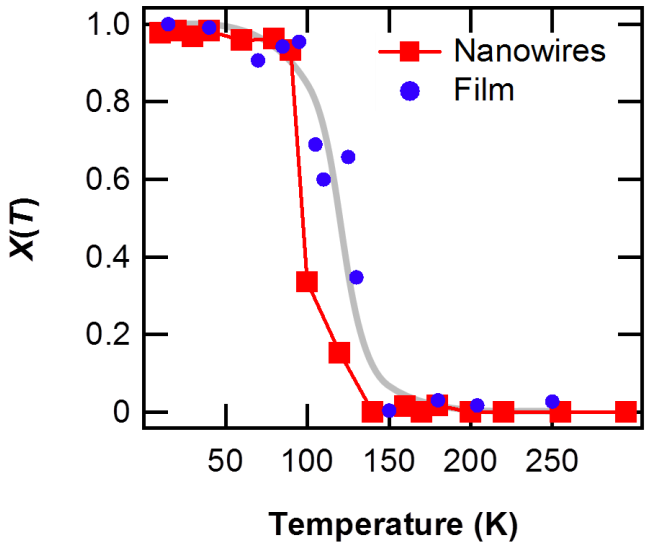

Fig. 4.8: Comparison of $X(T)$ result for the LPCMO nanowires sample (red squares) and that for the LPCMO film (blue dots). The light grey line is the guide for eyes.

As an effort to explain this observed result, we conducted the simulation for checking the effect of domain reduction in a nanowire compared with a thin film by using the random resistor network model [19-22]. The calculation was conducted for a ($n \times m$) lattice where each element in the lattice represented a metal or insulator

domain with the different conductivity. Here, the domain reduction was taken into account by changing the value of n while value of m was fixed at 50. Therefore $n \times m$ =1×50 lattice demonstrated a nanowire with the wire-width equals to the size of one single domain, and $n \times m$ =100×50 lattice corresponded to a film. In the simulation, other parameters such as the property of metallic and insulator domain, or the transition temperature were also similar in all calculations. As the temperature increased, the number of transited domains at each temperature was randomly calculated and correspondingly, the value of metal fraction $X(T)$ was estimated. Figure 4.9 shows the simulated $X(T)$ curves in two typical cases of n = 1 (red) and n = 100 (blue), in which the temperature in n = 1 case was offset by 10 K for an easier observation. Here the step change in $X(T)$ curve of n = 1 was observed while the gradual behavior was seen for that of n = 100. This calculation was consistent with the evaluated data in fig. 4.8, therefore we could conclude that the step change in $X(T)$ for the nanowires sample originated from the reduction of domain.

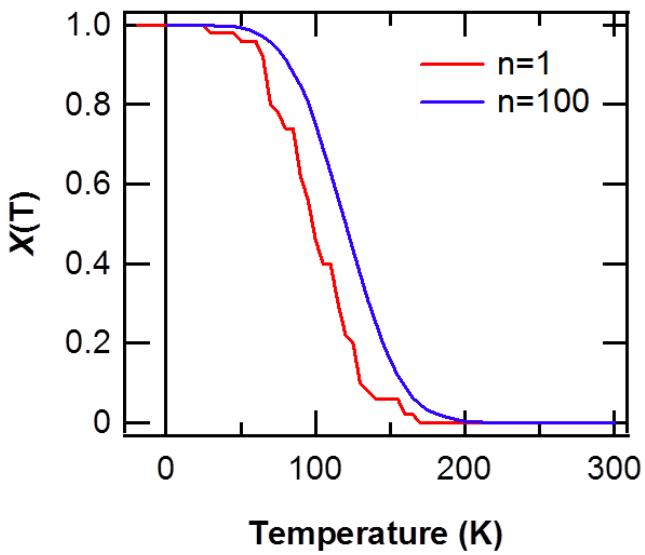

Fig. 4.9: Simulated $X(T)$ behaviors for a nanowire (n=1) in comparison with a film (n=100).

Concurrently, we could numerically estimate dc conductivity $\sigma_0(T)$ by extrapolating the $\sigma_{THz}(\omega,T)$ curves to 0 THz using Eq. (4.1). The result displayed in Fig. 4.10 shows about three orders of magnitude change of the dc conductivity of through the MIT process (red dots). This result closely reproduced the $\sigma_{dc}(T)$ curve (blue line) obtained by the 2-probe electric measurement. Here, the deviation of the $\sigma_0(T)$ curve and $\sigma_{dc}(T)$ curve was observed with the faster decrease of $\sigma_0(T)$ as the temperature increased. This might originate from the drastic change of metallic domains to insulator domains as observed in Fig. 4.9. The further investigation is required to give a thoroughly elucidation for this result.

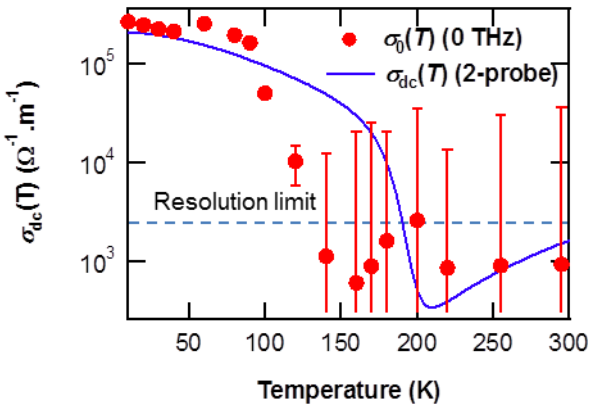

Fig. 4.10: Temperature dependence of dc conductivity (red dots) estimated from THz-TDS (which is the THz conductivity at frequency of 0 THz) in comparison with that obtained from the 2-probe measurement (blue line).

In this study, I demonstrated the investigation of nanopeculiar property of the domain evolution $X(T)$ and its correlatation with the dc conductivity $\sigma_{dc}(T)$ for a nanowires sample by using THz-TDS. This opens up a novel approach to investigate the peculiar properties in nanomaterials toward the application in nanodevices [9]. Moreover, this approaching route is also applicable for other mixed-phase nanostructured materials of not only the strongly correlated nanostructures, but also

the core-shell semiconductor nanocrystals [23], or the nanoscale electrically mixed nano-hetero-material [24,25].

4.5 Conclusion

In summary, I have fabricated the high density LPCMO nanowires over a large area of more than 3 mm^2 with the single phase crystallinity. The structure effect could be observed in the 100-nm-width and 60-nm-heigh LPCMO nanowires sample at 10 K which showed the change of conductivity curve from metallic to dielectric behavior as the wire alignment changed from parallel to perpendicular to the polarization of THz pulse. This feature is promising for applications in the tunable filters in THz region using phase-separated manganites systems. The exclusion of structure effect was successful so that the intrinsic conductivity curves for this sample could be obtained that followed the IMT process. The intrinsic electric transport properties could be obtained by fitting THz conductivity curves with the insulator-metal composite model. The domain evolution and dc conductivity could simultaneously evaluate. Further studies in the natural LPCMO nanowires metamaterials in the terahertz frequency region are promising for applications of tunable electro-optical devices.

4.6 References

1. A. P. Ramirez, J. Phys.: Condens. Matter **9** (1997) 817
2. J. M. D. Coey, M. Viret, and S. von Molnár, Adv. Phys. **48** (1999) 167
3. M. K. Wu, J. R. Ashburn, C. J. Torng, P. H. Hor, R. L. Meng, L. Gao, Z. J. Huang, Y. Q. Wang, and C. W. Chu., Phys. Rev. Lett. **58** (1987) 908
4. T. V. A. Nguyen, A. N. Hattori, Y. Fujiwara, S. Ueda, H. Tanaka, Appl. Phys. Lett. **103** (2013) 223105
5. M. Uehara, S. Mori, C. H. Chen, and S.-W, Cheong, Nature **399** (1999) 560
6. T. V. A. Nguyen, A. N. Hattori, M. Nagai, T. Nakamura, K. Fujiwara, M. Ashida, H. Tanaka, Appl. Phys. Lett. **105** (2014) 023502
7. H. Takami, T. Kanki and H. Tanaka, Appl. Phys. Lett. **104** (2014) 023104
8. Y. Yanagisawa, H. Tanaka, T. Kawai, L. Pellegrino, Appl. Phys. Lett. **89** (2006) 253121
9. H. Takagi, H. Hwang, Science **327** (2010) 1601
10. J. Cao, E. Ertekin, V. Srinivasan, W. Fan, S. Huang, H. Zheng, J. W. L. Yim, D. R. Khanal, D. F. Ogletree, J. C. Grossman, J. Wu, Nature Nanotechnology **4** (2009) 732
11. Y. Minowa, T. Fujii, M. Nagai, T. Ochiai, K. Sakoda, K. Hirao, K. Tanaka, Optics Express **16** (2008) 4785
12. D. Grischkowsky, S. Keiding, Appl. Phys. Lett. **57** (1990) 1055
13. I. G. Austin, N. F. Mott, Adv. Phys. **18** (1969) 41
14. N. Kida, M. Hangyo, M. Tonouchi, Phys. Rev. B **62** (2000) R11965
15. F. Wooten, *Optical Properties of Solids*, Academic Press, New York and London (1972) p.52

16. Y. Akishige, T. Fukatsu, M. Kobayashi, E. Sawaguchi, Jour. Phys. Soc. Jpn. **54** (1985) 2323
17. M. Dressel, G. Grüner, *Electrodynamics of Solids*, Cambridge University Press, Cambridge (2002) p.329
18. A. Pimenov, S. Tachos, T. Rudolf, A. Loidl, D. Schrupp, M. Sing, R. Claessen, V. A. M. Brabers, Phys. Rev. B **72** (2005) 035131
19. T. Nakamura, A. N. Hattori, T. V. A. Nguyen, K. Fujiwara, H. Tanaka, Appl. Phys. Express, **8** (2015) 073201
20. A. N. Hattori, Y. Fujiwara, K. Fujiwara, T. V. A. Nguyen, T. Nakamura, M. Ichimiya, M. Ashida, H. Tanaka, Nano letters, **15** (2015) 4322
21. H. Takami, K. Kawatani, H. Ueda, K. Fujiwara, T. Kanki, H. Tanaka, Appl. Phys. Lett. **101** (2012) 263111
22. H. Takami, Doctoral thesis, 2014, Osaka University, Japan
23. C. S. Bell, S. S. Yu, T. D. Giorgio, Small **7** (2011) 1158
24. P. H. Jampany, K. Kadakia, D. H. Hong, R. Epur, J. A. Poston, A. Manivannan, P. N. Kumta, J. Electrochem. Soc. **160** (2013) A1118
25. L. Zhang, T. Liu, K. Liu, L. Han, Y. Yin, C. Gao, Nano Lett. **15** (2016) 4448

CHAPTER 5

Colossal magnetoresistive (La,Pr,Ca)MnO_3 nanobox array structures constructed by the three-dimensional nanotemplate pulsed laser deposition technique

Abstract

Precisely size-controlled and crystalline $(La_{0.275}Pr_{0.35}Ca_{0.375})MnO_3$ (LPCMO) nanobox array structures were fabricated down to 30 nm in wall-width by the three-dimensional nanotemplate pulsed laser deposition technique. The hard X-ray photoemission spectroscopy in LPCMO nanobox array structures showed the existence of the satellite on the Mn $2p_{3/2}$ peak at 203 K with a higher intensity than that in the LPCMO film even at 153K. This result indicated that the insulator - metal transition (IMT) in the nanobox array structures occurred at the higher IMT temperature.

5.1 Introduction

Strongly correlated transition metal oxides have attracted much attention because of their huge external-field-induced response originating from the strong coupling between spin, charge, and orbital (lattice) degrees of freedom [1]. An illustrative example can be found in the perovskite $(La,Pr,Ca)MnO_3$ system with numerous gigantic properties, such as colossal magnetoresistance (CMR) with metal/ferromagnetic-insulator/antiferromagnetic transition. During the metal-insulator transition, the ferromagnetic metal (FMM) and the charge ordering insulator (COI) phases coexist in the state of electronic/spin domains in nano-scale [2,3]. Thus nanostructuring the strongly correlated $(La,Pr,Ca)MnO_3$ is a frontier to deliver promising functional nano-materials.

To investigate and mastermind these specific properties in the nano-sized structures, both the precise size control of nanostructures and the understanding of

their physical properties are indispensable. Recently, the nanofabrication technique, namely the three-dimensional (3D) nanotemplate pulsed laser deposition (PLD) technique [4-7] have been established by the combination of the PLD technique with the nano imprint lithography (NIL) technique. This technique permits us to produce highly crystallized nanostructures whose wall-width is well defined as the 10-nm scale on a large area while maintaining initial template positions and shapes exactly.

5.2 Purpose

In this study, I will show how to construct the accurately wall-width-controlled and well-aligned $(La_{0.275}Pr_{0.35}Ca_{0.375})MnO_3$ (LPCMO) nanobox array structures, abbreviated to nanoboxes using the 3D nanotemplate PLD technique. The fabricated nanostructures had the crystal quality as good as the epitaxial film [4-7]. The hard X-ray photoemission spectroscopy (HX-PES) measurements, that enable the investigation of the true bulk electronic structure up to the probe depth of about 6 nm [8], were performed on nanoboxes for investigating their transport properties without electrodes. The $(La_{0.275}Pr_{0.35}Ca_{0.375})MnO_3$ stoichiometry was chosen to balance between the CMR property and the insulator-metal transition (IMT) temperature T_C [2]. These results will be presented in next part. The advantage of nanoboxes is that the large numbers of the well-defined ultra-narrow nanowall structures can be compactly stored with the high packing density, which warrants the measurement at a high signal-to-noise ratio.

5.3 Experiment

In this study, the LPCMO nanoboxes were fabricated on a MgO(001) substrate using the 3D nanotemplate PLD technique. The fabrication process for the LPCMO nanoboxes is summarized in the schematic image in figure 5.1.

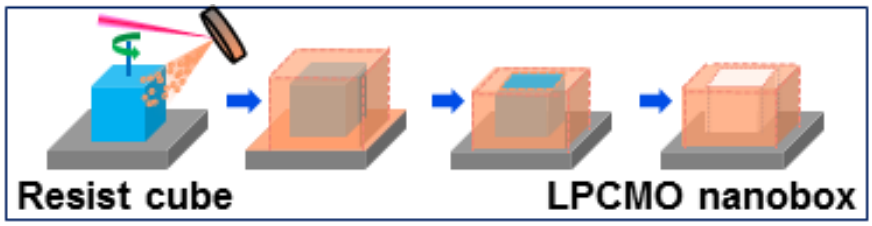

Fig. 5.1: Schematic image for the fabrication procedure of the LPCMO nanoboxes.

Firstly, the MgO(001) substrate was patterned with the organic resist cubes by the NIL technique. Then, the LPCMO was deposited by the PLD technique on the four side-surfaces of the resist cube at room temperature (RT). The LPCMO nanoboxes were obtained in a large area (~20 mm^2) after the LPCMO top layer and the inner core resist were removed. The detail procedure was described elsewhere [6]. To improve the crystallinity, the post-annealing process was fulfilled at 1270 K under the oxygen pressure of 1 Pa. The LPCMO films were fabricated on MgO(001) and SrTiO3(001) (STO) substrates as references [9]. The field-emission scanning electron microscope (SEM, JSM-7001, JEOL) and the X-ray diffraction measurement (XRD, Smart Lab, Rigaku) were performed at RT. The temperature dependence of films' resistivity, ρ(T) was measured using a physical property measurement system (Quantum Design). The Mn 2p core-level spectra were obtained at the undulator beamline BL15XU [10] of SPring-8 with the excitation photon energy of 5950 eV. The total energy resolution was 230 meV. The measurement temperature was ranged from 20 K to 300 K [11]. The photoemission peaks were fitted with Voigt functions after subtracting the Shirley-type background [12], and the fitting errors were always less than 10%.

5.4 Results and Discussion

This part, I will introduce the conductivity properties of LPCMO nanoboxes obtaining from the Mn core-level spectroscopy.

5.4.1 Highly crystallized and precisely-size-controlled LPCMO nanoboxes

Using the 3D nanotemplate PLD technique, I could obtain highly crystallized LPCMO nanoboxes with the width was precisely controlled. Figure 5.2 shows a typical SEM image of LPCMO nanoboxes with 100-nm wall-width and 400-nm height. The wall-width of nanoboxes had been accurately controlled in a range from 160 nm down to 30 nm by changing the deposition time as presented in figure 5.3.

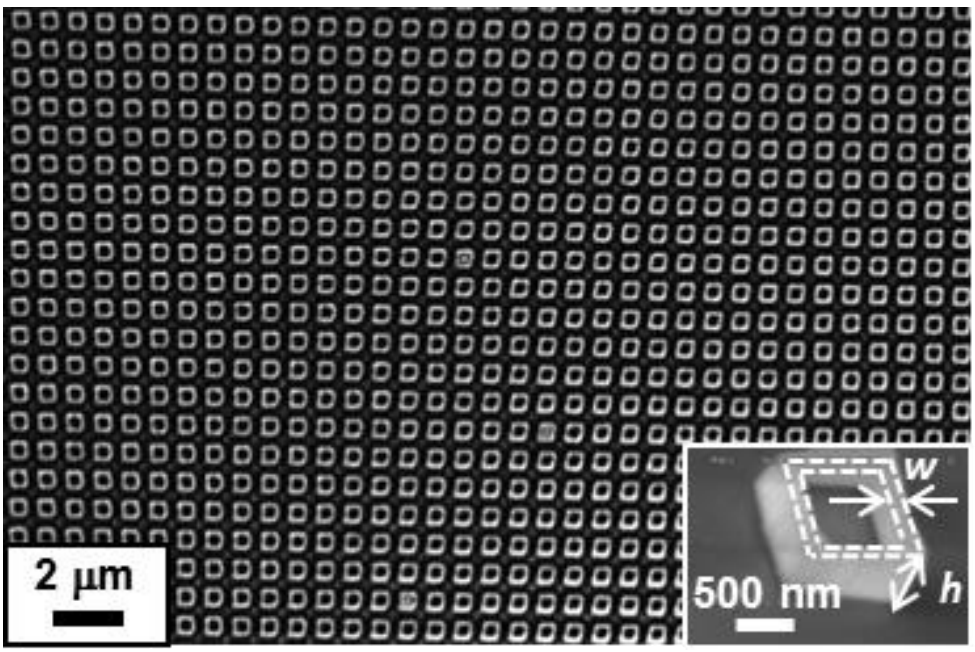

Fig. 5.2: Typical SEM image of LPCMO nanoboxes with 100-nm wall-width and 400-nm height.

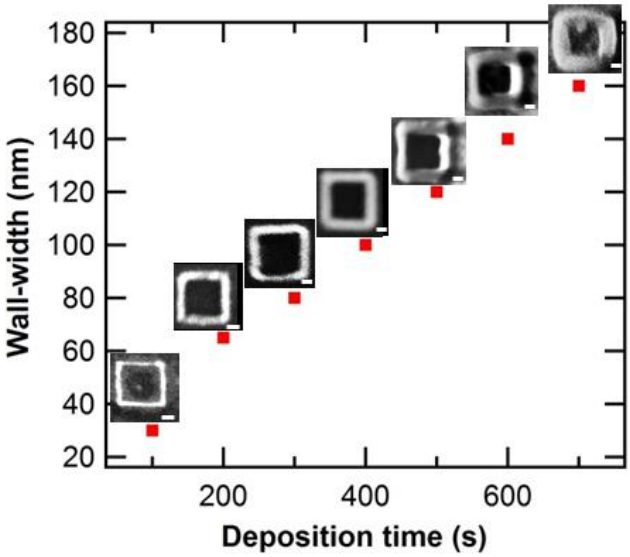

Fig. 5.3: The relationship between the wall-width of the LPCMO nanoboxes and the deposition time. The scale bars in inset SEM images correspond to 100 nm.

Figure 5.4 exhibits the XRD curves of 160-nm wall-width LPCMO nanoboxes, named NB_{MgO}, and 300-nm thickness LPCMO film on the MgO(001) substrate, named F_{MgO}. It can be seen that the NB_{MgO} sample had similar crystallinity to that of F_{MgO} with the diffraction peaks at $2\theta = 23.06^{o}$, 32.84^{o}, 47.04^{o} in 001, 110, and 002 planes of a pseudo-cubic perovskite unit cell, respectively. Similar results for other nanobox samples with different wall-widths had also been observed. The smaller peaks' intensity in the NB_{MgO} sample can be attributed to its much smaller volume. The 0.131^{o}-shift of 002 peak in the NB_{MgO} sample toward a smaller angle was typically observed (inset of figure 1 (c)). The estimated out-of-plane lattice parameters (*c* lattice) of NB_{MgO} and F_{MgO} samples were 0.3879 nm and 0.3869 nm, respectively. This implied the *c* lattice elongation in the NB_{MgO} sample.

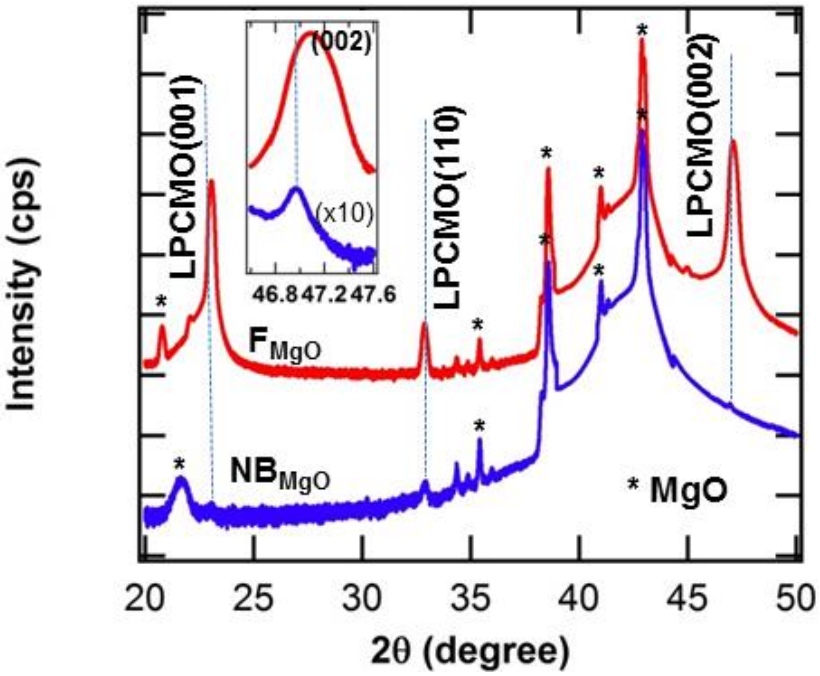

Fig. 5.4: XRD curves of NB_{MgO} and F_{MgO} samples. The inset is the magnified curves at 002 peak.

5.4.2 Conductivity properties of LPCMO nanoboxes investigated using Mn 2p core-level spectra

As a reference to discuss the electronic property of the nanoboxes, I investigated the relationship between HX-PES spectra and the electrical conductivity in LPCMO thin film samples

5.4.2.1 Conductivity properties of LPCMO film

Figure 5.5 displays the Mn 2p core-level HX-PES spectra of the F_{MgO} sample in the cooling process.

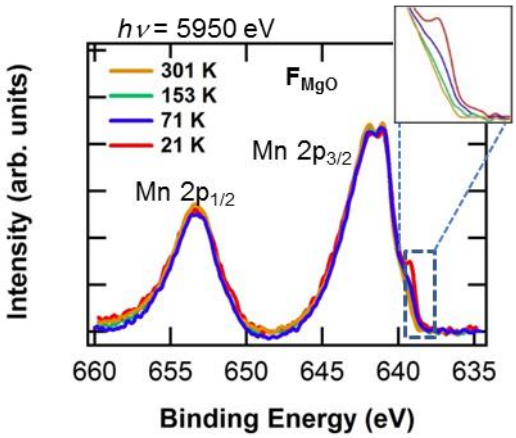

Fig. 5.5: Mn 2p core-level spectra of the F_{MgO} sample at different temperatures in the cooling process.

In fig. 5.5, it can be seen that the Mn 2p spectrum consists of two main peaks at 653.3 eV (Mn $2p_{1/2}$) and 641.5 eV (Mn $2p_{3/2}$). Notably, near the Mn $2p_{3/2}$ main peak in the low binding energy, a satellite peak at about 639.4 eV, which revealed the intrinsic electronic state of the manganite system, was observed. It is experimentally proposed that the area intensity of the satellite peak (I_s) was quantitatively attributed to electronic and magnetic properties [13].

Namely,

$$I_S(T) \propto D(E_F, T) \sim \sigma(T) \quad (T < T_C) \tag{5.1}$$

where $D(E_F,T)$, and $\sigma(T)$ are the density of states at the Fermi level and the electric conductivity, respectively. In the magnified image in figure 5.5, we can see the increase of the satellite peak with the temperature decrease while the spectral shape of the Mn $2p_{3/2}$ main peak did not show any significant change in the whole temperature range.

Let's discuss the relationship between the $\sigma(T)$ and $I_s(T)$ curves in the F_{MgO} sample, as expressed in Eq. (5.1). The conductivity $\rho(T)$ curve in the cooling process (figure 5.6) shows the transition from COI to FMM through the critical temperature

T_C of 75 K. Using this $\rho(T)$ curve, I could estimate the conductivity curve $\sigma(T)$ at temperatures below T_C. The values of $\sigma(T)$ above T_C were assumed to be zero (dash line) because of its insulating behavior ($D(E_F)$~0). Then the normalized conductivity $\sigma(T)$ and the $I_s(T)$ were plotted in figure 5.7. Here, the I_s values were estimated by normalizing with the Mn $2p_{3/2}$ peak. The I_s values at the temperatures above T_C were very small, whereas they increased steeply below T_C. The obtained results showed that the increasing tendency of the $I_s(T)$ tracks to the IMT process in the sample.

The competition between COI and FMM can be seen as the $\sigma(T)$ change (figure 5.6). When the temperature decreased, the FMM phase started growing within the COI host and the population of the FMM correspondingly increased. Then, the FMM phase became dominant at low temperatures. The accelerating of the I_s value as the temperature declined could be considered as a result of the development of the metallicity, *i.e.*, the electric conductivity. The clear similar tendency of $I_s(T)$ and $\sigma(T)$ curves in figure 5.7 could support the validity of Eq. (5.1). I can conclude that the temperature dependence of $I_s(T)$ reflects the conductivity change relating to the IMT in LPCMO system. The similar results as shown in figures 5.8 and 5.9 for the LPCMO film on the STO(001) substrate, named F_{STO}, with the T_C of 210 K could further support my conclusion.

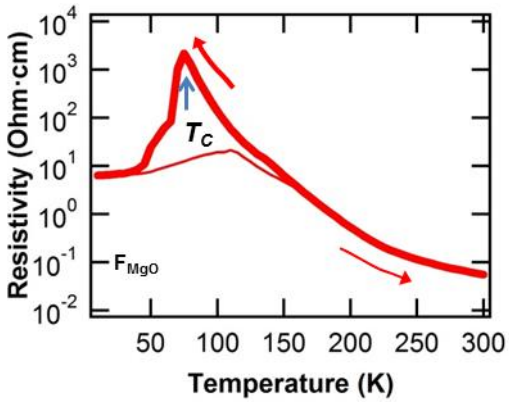

Fig. 5.6: The temperature dependence of the resistivity for the F_{MgO} sample.

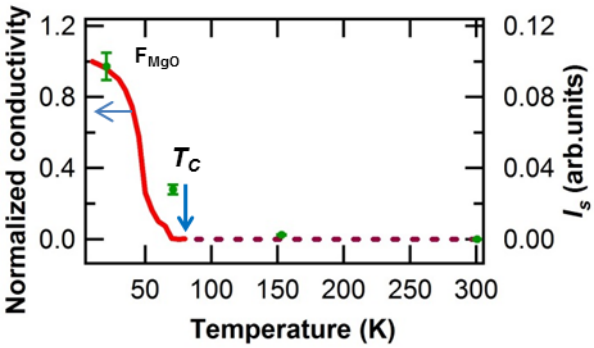

Fig. 5.7: The temperature dependence of I_s (green solid circles) in comparison with the normalized conductivity (lines) of the F_{MgO} sample in the cooling process. Supposing that at 300 K the number of the FMM phase was so small that the I_s value could be negligible.

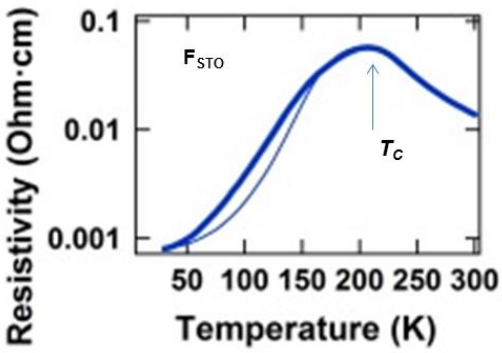

Fig. 5.8: The temperature dependence of the resistivity for the F_{STO} sample.

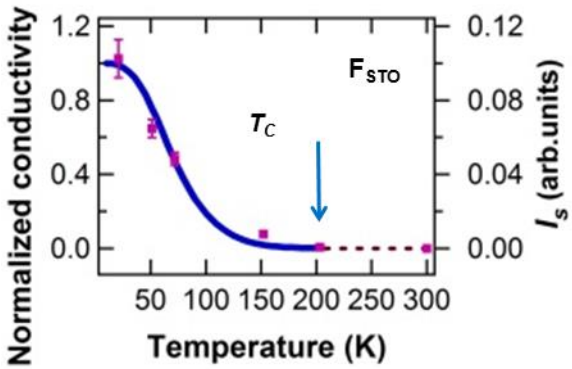

Fig. 5.9: The temperature dependence of I_s (green solid circles) in comparison with the normalized conductivity (lines) of the F_{STO} sample in the cooling process. Supposing that at 300 K the number of the FMM phase was so small that the I_s value could be negligible.

5.4.2.2 Conductivity properties of LPCMO nanoboxes investigated using Mn 2p core-level spectra

Now, I discuss the electric property of the nanoboxes sample. Figure 5.10 exposes the Mn 2p core-level spectra of NB_{MgO} sample at different temperatures. I could clearly observe the existence of the satellite peak at 203 K, whose estimated I_s value is 19 times and 6 times higher than those of the F_{MgO} sample at 153 K, and of the F_{STO} sample at 152 K, respectively.

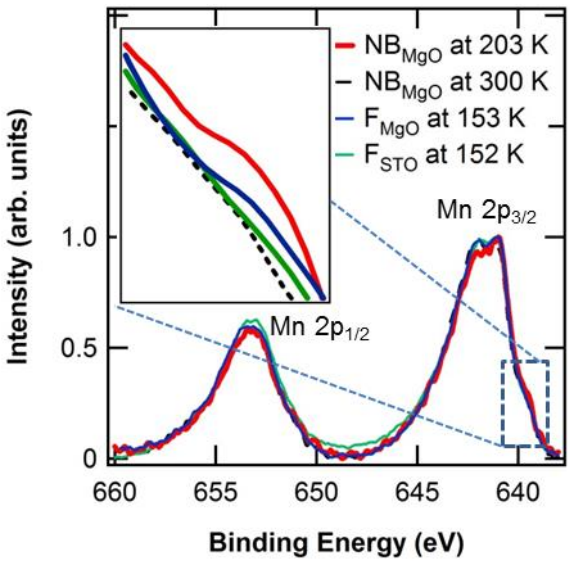

Fig. 5.10: Mn 2p core-level spectra of the NB_{MgO} sample at 203 K and 300 K in comparison with those of F_{MgO} and F_{STO} samples at 153 K and 152 K, respectively.

The $I_s(T)$ curve for the NB_{MgO} sample is summarized in the figure 5.11 in comparison with that for the F_{MgO} sample. Since the I_s behavior directly reflect the electric conductivity change through the IMT as shown in Eq. (5.1), I could conclude that the earlier appearance of satellite peak in NB_{MgO} sample corresponds to its higher T_C than that in F_{MgO} sample. This conclusion is opposite from the case of ultra-thin oxide films on the substrates which tend to be insulating [15] because the nanoboxes

had the freestanding structure and only their bottoms were contacted with the MgO substrate surface. Thus, there is scarcely substrate-induced strain between nanoboxes and the substrate. As an origin of the enhanced metalicity, i.e., the higher T_C in the nanoboxes, two possibilities could be considered: (1) the strain effect [14-18] by the complex 3D structures and (2) the oxygen over-doping due to cationic vacancies.[19] It was reported that the tensile strain decreases T_C through a reduction of the transfer integral in the manganite systems [14-16]. Actually, the *c* lattice elongation in NB_{MgO} sample suggesting the in-plane compress strain in the figure 1 (c) supports the possibility (1). On the other hand, the Mn 2p core-level spectra in fig. 5.5 and fig. 5.10 are against the possibility (2) because the positions of Mn $2p_{3/2}$ main peaks were similar in NB_{MgO} and F_{MgO} samples. Therefore, the possibility (1) involving in the strain effect is the suitable explanation in this stage.

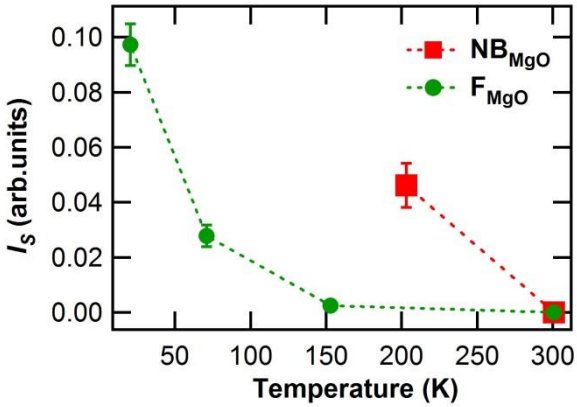

Fig. 5.11: The temperature dependence of the I_s for the NB_{MgO} sample (red squares) compared with those for the F_{MgO} sample (green solid circles) in the cooling process. The corresponding dashed lines between points are the guides for eyes.

5.5 Conclusion

In summary, I have fabricated the accurately wall-width-controlled LPCMO nanoboxes as small as 30 nm in wall-width with high integrated array structures. The HX-PES experiment using the satellite of the Mn $2p_{3/2}$ peak, without attaching electrodes as must be done for the electric conductivity measurement, revealed that these manganite nanobox array structure exhibited IMT functionality. In detail, nanoboxes showed the IMT at the higher temperature than that in the film. These results indicate that the well-aligned and easily-prepared, highly-integrated CMR manganite 3D nanoboxes have the possibility to offers a way to tune physical properties in CMR oxides. The 3D nanotemplate PLD technique can construct the tunable wall-width or the diameter of the nanoboxes, and the distance between boxes down to 10 nm so that this technique will open up a way of not only tunable superior electronic/magnetic properties in correlated oxides, but also nano-devices with the designed location of nano-materials, such as magnetically and/or temperature tunable photonic crystals taking the advantage of the huge electronic/spintronics phase transition.

5.6 References

1. M. Imada, A. Fujimori, and Y. Tokura, Rev. Mod. Phys. **70** (1998) 1039.
2. M. Uehara, S. Mori, C. H. Chen, and S.-W, Cheong, Nature **399** (1999) 560.
3. L. Zhang, C. Israel, A. Biswas, R. L. Greene, and Alex de Lozanne, Science **298** (2002) 805.
4. T. Kushizaki, K. Fujiwara, A. N. Hattori, T. Kanki, and H. Tanaka, Nanotechnology **23** (2012) 485308.
5. A. N. Hattori, A. Ono, and H. Tanaka, Nanotechnology **22** (2011) 415301.
6. A. N. Hattori, M. Ichimiya, M. Ashida, and H. Tanaka, Appl. Phys. Express **5** (2012) 125203.
7. Y. Fujiwara, A. N. Hattori, K. Fujiwara, and H. Tanaka, Jpn. J. Appl. Phys. **52** (2013) 015001.
8. M. V. Veenendaal, Phys. Rev. B **74** (2006) 085118.
9. LPCMO films on MgO(001) and STO(001) were deposited at 1073 K under the oxygen pressure of 1 Pa.
10. S. Ueda, Y. Katsuya, M. Tanaka, H. Yoshikawa, Y. Yamashita, S. Ishimaru, Y. Matsushita, and K. Kobayashi, AIP Conf. Proc. **1234** (2010) 403.
11. The NB_{MgO} sample had strong charge-up effect because of the bare region on the insulating MgO(001) substrate surface. Thus, at lower temperature (below 200 K), the spectra for NB_{MgO} sample could not be obtained.
12. J. E. Castle, and A. M. Salvi, J. Vac. Sci. Technol. A **19** (2001) 1170.
13. H. Tanaka, Y. Takata, K. Horiba, M. Taguchi, A. Chainani, S. Shin, D. Miwa, K. Tamasaku, Y. Nishino, T. Ishikawa, E. Ikenaga, M. Awaji, A. Takeuchi, T. Kawai, and K. Kobayashi, Phys. Rev. B **73** (2006) 094403.

14. M. Izumi, Y. Konishi, T. Nishihara, S. Hayashi, M. Shinohara, M. Kawasaki, and Y. Tokura, Appl. Phys. Lett. **73** (1998) 2497.
15. R. B. Praus, B. Leibold, G. M. Gross, and H.-U. Habermeier, Appl. Surf. Sci. **138-139** (1999) 40, and references therein.
16. B. Vengalis, A. Maneikis, F. Anisimovas, R. Butkuté, L. Dapkus, and A. Kindurys, J. Magn. Magn. Mater. **211 (**2000) 35.
17. T. Z. Ward, S. Liang, K. Fuchigami, L. F. Yin, E. Dagotto, E. W. Plummer, J. Shen, Phys. Rev. Lett. **100** (2008) 247204.
18. I could not deny the possibility of the reemergence of the second IMT behavior involving in the spatial confinement in the nanostructures as reported in Ref. [17] because of the data limitation at low temperature. However, the further discussion is beyond the purpose of this paper.
19. P. Murugavel, J. H. Lee, Jong-Gul Yoon, T. W. Noh, J.-S. Chung, M. Heu, and S. Yoon, Appl. Phys. Lett. **82** (2003) 1908.

CHAPTER 6

General conclusion

I investigated the electrical transport properties which exhibited the correlation between the domain revolution and dc electric conductivity in phase-separated manganite by using terahertz time domain spectroscopy (THz-TDS).

In chapter 3, I established a procedure to estimate the electrical transport properties (the domain revolution $X(T)$ and the dc conductivity $\sigma_{dc}(T)$) for a (La,Pr,Ca)MnO_3 (LPCMO) film by using THz-TDS. At first, the frequency dependent THz conductivity at different temperatures ($\sigma_{THz}(\omega,T)$ curves) could be obtained using the THz-TDS measurements. Then, overcoming the lack of the existing models, I proposed the composite model to explain the change of $\sigma_{THz}(\omega,T)$ behavior through the IMT for this mix-phase material. This model enabled a reliable investigation of $X(T)$ and $\sigma_{dc}(T)$ for the LPCMO film in a non-contact manner. This technique is applicable for the electrically phase-separated materials, especially the phase-separated nanostructures.

In the chapter 4, I applied this procedure to investigate the transport dynamics in a LPCMO nanowires sample through the IMT using the THz-TDS. The external structure effect could be excluded by aligning the high-density nanowires parallel with the polarization of THz pulse. Then I could obtain their intrinsic conductivity behavior change following the MIT process in the sample. The $X(T)$, estimated by fitting $\sigma_{THz}(\omega,T)$ curves with my proposed insulator-metal composite model, revealed the change of electronic domain from insulator to metal with the decrease of temperature. Simultaneously the $\sigma_{dc}(T)$ for nanowires could be evaluated without attaching electrodes.

In chapter 5, I successfully produced the LPCMO nanobox array structures (nanoboxes) with precise control their wall-width down to 30 nm using an original three-dimensional (3D) nanotemplate pulsed laser deposition (PLD) technique. This can be considered as a development of nanostructure fabrication which enables the confinement of a single nano-electronic domain to employ its specific sharp single-domain insulator metal transition. Also, the study on hard X-ray photoemission spectroscopy for LPCMO nanoboxes revealed their peculiar IMT property in comparison with that of a LPCMO thin film. This (3D) nanotemplate PLD technique is a powerful technique for fabricating 3D nanostructures towards their future applications in nano-oxide-electronics.

Through a sequence of experiments of THz-TDS for mix-phase manganite film and nanowires structure in this thesis, I demonstrated the significance of my research on establish an efficient way to investigate the correlation between the nanoscale domain evolution and dc electric conductivity in a phase-separated manganite by explaining the temperature-induced change in THz conductivity behavior based on my proposed composite model. This novel established technique is also applicable for a direct estimation of the electrical transport properties in other mix-phase nanostructured materials of not only the strongly correlated nanostructures, but also the core-shell semiconductor nanocrystals, the high-temperature alloy resistor composed of metal nanopartical and semiconductor matrix, and the variety of nanoscale electrically mixed nano-hetero-materials whose peculiar properties are promising for future nano-devices.

CHAPTER 7

Appendix

7.1 Analyzing procedure [1-9]

In my research, the THz pulse was employed to study the THz respond of the mix-phase manganite after the excitation. In short, the THz pulse passing through the sample will be used to calculate its THz conductivity. Now I will explain more detail about this analyzing procedure.

Generally, the description of an optical pulse propagation, obtained from Maxwell's equations [1], whose the electric field of a short light pulse to propagate along *z* axis and to be linearly polarized along *x* axis is:

$$E(r,t) = \frac{1}{2}a(z,t)F(x,y)\,\mathrm{e}^{i(k_0 z - w_0 t)}$$

here $a(z,t)$ is the temporal envelope, $F(x,y)$ is spatial envelope of the pulse (or wave packet); $\nu_0 = {}^{\omega_0}/_{2\pi}$ is the frequency and $k_0 = {}^{\omega_0 n_{(\omega_0)}}/_{c}$ determines the wavelength ($\lambda_0 = {}^{2\pi}/_{k_0}$) of the pulse.

This pulse, after passing through the sample will show the change in the amplitude and the phase. In the terahertz time domain spectroscopy (THz-TDS), both of these changes in time domain can be detected in the waveforms and then they are transformed to the frequency domain using a fast Fourier transformation (FFT) to obtain power spectra (show the change of amplitude) and phase spectra (show the change of phase) in frequency domain. Figure 7.1 demonstrates the analyzing procedure to obtain THz conductivity in my research. For the film sample on a substrate, the THz conductivity of the film is obtained after subtracting the contribution from the substrate using one media approximation.

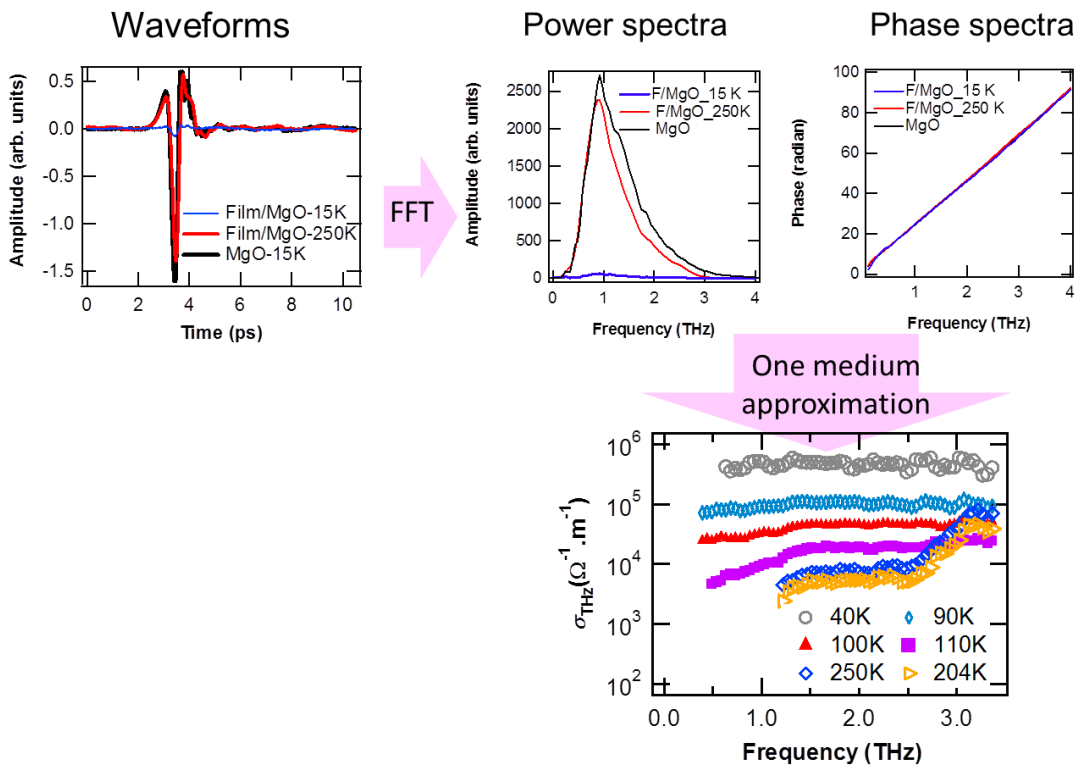

Fig. 7.1: Analyzing procedure to obtain THz conductivity curve.

7.2 Analyzing code

In this part, I show the analyzing code for obtaining THz conductivity from the initial waveforms. This code has been written in Igor program by Professor M. Nagai of Graduate School of Engineering Sciences, Osaka University; and I have modified some parts in the code.

Procedure

```
// This part is used for FFT transformation to the frequency - Anh

Macro powerspectrum(inw, baseline)
 String inw
 Variable/D baseline=0
 Prompt inw, "select wave",popup WaveList("*", ";","WIN:")
 Prompt baseline, "input baseline"
 String outf=inw+"_FFT"
 String outw=inw+"_I"
 String outp=inw+"_p"
 String outc=inw+"_c"
 Variable/C mag
 Variable num,num2
 silent 1
 PauseUpdate

 if (exists(inw)==1)
 Duplicate/R=(xcsr(A),xcsr(B))/O $inw $outf
 $outf-=baseline    // set offset value
 InsertPoints 0,(pcsr(A)-1), $outf
 InsertPoints pcsr(B)+1,(2048-pcsr(B)), $outf

 FFT $outf
 num=numpnts($outf)
 Make/N=(num)/D/O $outw, $outp
 SetScale/P x 0,(1/num/deltax($inw)/2),"", $outw, $outp
 print xcsr(A), xcsr(B), deltax($inw)

 iterate(num)   // calculating power spectrum and phase
  mag=$outf[i]
  $outw[i]=cabs(mag)^2
  if (real(mag)<0)
     $outp[i]=atan(imag(mag)/real(mag))+Pi
  else
   $outp[i]=atan(imag(mag)/real(mag))
  endif
  if ($outp[i]<0)
   $outp[i]+=2*Pi
  endif
 loop
```

Templates Procedures

Procedure

```
  // phase control
 Duplicate/O $outp $outc
 iterate(num-1)
  num2=num-1-i
  $outc[num2]=$outp[num2]-$outp[num2-1]
  if ($outc[num2]>4)
    $outc[num2]=0
    $outc[num2,num-1]-=2*Pi
    else
    if ($outc[num2]<-0.8)
      $outc[num2]= 0
      $outc[num2,num-1]+= 2*Pi
    else
      $outc[num2]=0
    endif
  endif
 loop

 $outp+=$outc
 Killwaves $outc

 else
   abort "You inputed wrong wavename!"
 endif
endMacro


macro matomete(vw)
 Variable/D vw
 String waven
 Variable Num=0, gotwave
 Silent 1
 PauseUpDate

 do
  waven= WaveName("",Num,1)
  gotwave=cmpstr(waven, "")
  if(gotwave!=0)
 powerspectrum(waven,vw)
  endif
  Num+=1
 while (gotwave)
endmacro
```

Templates Procedures

Procedure

```
Function mytds_s1(w, x1, x2)      // analysis with assumption of single pass
    Wave w        //w[0]=thickness um  w[1]=freq THz  w[2]=T  w[3]=phase
    Variable x1,x2  // index (real and imaginary)
    Variable/C x    //complex index
    Variable AA,BB
    AA=300/(2*Pi*w[0]*w[1])
    x=cmplx(x1,x2)
    BB=w[3]-imag(r2polar(x/(x+1)^2))
    return 1-x1+AA*BB
End

Function mytds_s2(w, x1, x2)      // analysis with assumption of single pass
    Wave w        //w[0]=thickness um  w[1]=freq THz  w[2]=T  w[3]=phase
    Variable x1,x2  // index (real and imaginary)
    Variable/C x    //complex index
    Variable AA,BB
    AA=300/(2*Pi*w[0]*w[1])
    x=cmplx(x1,x2)
    BB=cabs(sqrt(w[2])/4/x*(x+1)^2)
    return x2+AA*ln(BB)
End


Function mytds_m1(w, x1, x2)    // analysis with assumption of multi-reflection
    Wave w  //w[0]=thickness um  w[1]=freq THz  w[2]=T  w[3]=phase
    Variable x1,x2 // index (real and imaginary)
    Variable x=w[1]
    Variable t=w[0]                          //thickness
    Variable/C n_f=cmplx(x1,x2)
    Variable/C n_s=cmplx(3.1,0)              // index of the substrate
    Variable/C r12,r23,t12,t23,prop_f, prop_d
    Variable/C ttt, deno, numer, t12t
    r12=(n_f-1)/(n_f+1)
    r23=(n_s-n_f)/(n_s+n_f)
    t12=2/(n_f+1)
    t23=2*n_f/(n_s+n_f)
    t12t=2/(n_s+1)
    prop_f=2*Pi*t*x/300*n_f*cmplx(0,1)
    prop_d=2*Pi*t*x/300*(n_f-1)*cmplx(0,1)
    numer=t12*t23*exp(prop_d)
    deno=1+r12*r23*exp(2*prop_f)
    ttt=numer/deno/t12t
    return magsqr(ttt)-w[2]
End
```

Templates Procedures

Procedure

```
Function mytds_m2(w, x1, x2)    // analysis with assumption of multi-reflection
    Wave w  //w[0]=thickness um  w[1]=freq THz  w[2]=T  w[3]=phase
    Variable x1,x2 // index (real and imaginary)
    Variable x=w[1]
    Variable t=w[0]                          //thickness
    Variable/C n_f=cmplx(x1,x2)
    Variable/C n_s=cmplx(3.1,0)              // index of the substrate
    Variable/C r12,r23,t12,t23,prop_f, prop_d
    Variable/C ttt, deno, numer, t12t
    r12=(n_f-1)/(n_f+1)
    r23=(n_s-n_f)/(n_s+n_f)
    t12=2/(n_f+1)
    t23=2*n_f/(n_s+n_f)
    t12t=2/(n_s+1)
    prop_f=2*Pi*t*x/300*n_f*cmplx(0,1)
    prop_d=2*Pi*t*x/300*(n_f-1)*cmplx(0,1)
    numer=t12*t23*exp(prop_d)
    deno=1+r12*r23*exp(2*prop_f)
    ttt=numer/deno/t12t/p2rect(cmplx(1,w[3]))
    return imag(r2polar(ttt))
End


Macro t2index(ww1,ww2,ww4, thickness,st, fn, in_n, in_k)
    String ww1,ww2,ww4  //1 trans,  2 phase,  ,  4 output
    Variable st=0,fn=128,  thickness=125
    Variable in_n=1.8, in_k=0.01
    Prompt ww1, "select wave of transmission (power)",popup WaveList("*", ";", "")
    Prompt ww2, "select wave of  phase shift",popup WaveList("*", ";", "")
    Prompt ww4, "set output wave strings"
    Prompt thickness, "set the thickness of the sample"
    Prompt st, "set the initial pixel"
    Prompt fn, "set the last pixel"
    Prompt in_n, "set initial real index for FindRoot"
    Prompt in_k, "set initial imaginary index for FindRoot"

    String ww5=ww4+"_n", ww6=ww4+"_k", ww3="para"
    Silent 1
    PauseUpDate
    Make/N=4/D/O $ww3
    $ww3[0]=thickness
```

Templates Procedures

Procedure

```
// if  you evaluate index in limited region, set the following 3 lines invalid
      Duplicate/O $ww1 $ww5, $ww6
       $ww5=NaN
       $ww6=NaN

      do
      $ww3[1]=pnt2x($ww1, st)
      if(pnt2x($ww1, st)>0)
            $ww3[2]=$ww1[st]
            $ww3[3]=$ww2[st]

// This part is used for calculating the THz conductivity from refractive index
//  choose the command (single pass or multi pass)
//          FindRoots/X={(in_n),(in_k)}/Q  mytds_s1, $ww3, mytds_s2, $ww3   // single-pass
            FindRoots/X={(in_n),(in_k)}/Q  mytds_m1, $ww3, mytds_m2, $ww3  //multi-pass

            $ww5[st]=W_Root[0]^2-W_Root[1]^2              //imaginary part
            $ww6[st]=1.1*10^2*W_Root[0]*W_Root[1]*x      //real part
//     If index is strongly dependent of frequency, set the following two lines valid
//          in_n=W_Root[0]
//          in_k=W_Root[1]
      endif
      st+=1
      while(st-fn-1)
endmacro
```

Templates Procedures Compile

Procedure

```
////////////////////////////////////////////
// This procedure is for systematical loading
// all files in one directry with two column data.
// This provedure is for IgorPro 4 for Windows.
//    created by M. Nagai on April, 1996,
//    modified on June. 10, 2012
////////////////////////////////////////////

Menu "Load Waves"
 "-"
 "Loading"
End

////////////////////////////////////////////
Proc Loading(cho_pro,thePath,wy_name)
 String cho_pro ="_FileName_"
 String thePath ="_New Path_"
 String wy_name =""
 Prompt cho_pro, "What you want to name waves?", popup "_FileName_"
 Prompt thePath, "Name of path containing data files", popup PathList("*", ";", "")+"_New Path_"
 Prompt wy_name, "Wave names of y"
 Silent 1        //      Now Data Loading...

 if (CmpStr(thePath, "_New Path_") == 0)
  NewPath/O data
  thePath = "data"
 endif

 if (exists("wave0")==0)
  if (CmpStr(cho_pro, "_FileName_") == 0)
    Load_o(thePath,wy_name)
  endif
 else
  Abort("Please rename wave0.")
 endif
end

////////////////////////////////////////////
```

Templates Procedures Compile

Procedure

```
////////////////////////////////////////////

Function Load_o(thePath,wy_name)
  String thePath
  String wy_name
  String fileName,wawawa
  Variable fileIndex=0, gotFile
  PauseUpDate

  do
    fileName = TextFile($thePath, fileIndex)
    gotFile = CmpStr(fileName, "")
    if (gotFile)
      LoadWave/G/P=$thePath/O/N=wave fileName
      wawawa=wy_name+fileName
      if (strsearch(wawawa,".",0)>-1)
        wawawa= wawawa[0,strsearch(wawawa,".",0)-1]
      endif
      rename wave0 $wawawa
    endif
    fileIndex += 1
  while (gotFile)
end

////////////////////////////////////////////
```

Templates Procedures Compile

Procedure

```
//////////////////////////////////////////////
// the value of each wave at special point
//  You can change the initial strings; outvalue and outname.
//////////////////////////////////////////////

Macro WaveDep_point(outvalue)
  String outvalue="Point", outname="Wave_Name"
  Prompt outvalue, "Enter the recorded wave name"
  Variable P=xcsr(A), gotwave,Num=0,datanum=0
  String wavenm
  silent 1
  PauseUpDate

//  if (CmpStr(CsrXWave(A),"") == 0)
//    Abort ("Set A-Cursor on the top graph.")
//  endif

  do       // count the number of wave on the active graph
    wavenm = WaveName("",datanum, 1)
    gotwave = CmpStr(wavenm, "")
    datanum += 1
  while (gotwave)

  Make/N=(datanum-1)/O/T  $outname    // make wave of file name
  Make/N=(datanum-1)/D/O $outvalue    // make recorded wave

  do
    wavenm = WaveName("",Num, 1)
    gotwave = CmpStr(wavenm, "")
    if (gotwave==1)
      $outvalue[Num]=$wavenm(p)
      $outname[Num]=wavenm
    endif
    Num += 1
  while (gotwave)
  print "x=",pcsr(A),"(",xcsr(A),"Pixel )    Recorded wave = ",outvalue," (N=",datanum-1,")"
  DoUpDate
endmacro

//////////////////////////////////////////////
```

Templates | Procedures | Compile

Procedure

```
////////////////////////////////////////////
// Max value of each wave at the range
// Max location of each wave at the range
// Intensity average of each wave at the range
//You can change the initial strings; outvalue and CFunc

////////////////////////////////////////////

Macro WaveDep_range(outvalue,CFunc)
  String outvalue="Range"
  String CFunc="_Avg Int_"
  Prompt CFunc, "Select Function",popup "_Max Int_;_Max Loc_;_Avg Int_"
  Prompt outvalue, "Enter the recorded wave name"
  String wname="Wave_Name",xwname
  Variable Pst=xcsr(A),Pfi=xcsr(B),gotwave,Num=0,datanum=0
  Variable/D StatFunc
  String wavenm

  silent 1
  PauseUpDate

//     if (CmpStr(CsrXWave(A),"")* CmpStr(CsrXWave(B),"")== 0)
//          Abort ("Set A- or B- Cursor on the top graph.")
//     endif
  do          //count the number of wave on the active graph
    wavenm = WaveName("",datanum, 1)
    gotwave = CmpStr(wavenm, "")
    datanum += 1
  while (gotwave)
  Make/N=(datanum-1)/O/T  $wname
  Make/N=(datanum-1)/D/O $outvalue
  do
    wavenm = WaveName("",Num, 1)
    gotwave = CmpStr(wavenm, "")
    if (gotwave==1)
      WaveStats /Q/R = (Pst, Pfi) $wavenm
      if (CmpStr(CFunc, "_Max Int_") == 0) //Maximum
        StatFunc= V_max
      endif
      if (CmpStr(CFunc, "_Max Loc_") == 0)//Maximum location
        xwname=XWaveName("",wavenm)
        if (CmpStr(xwname, "") == 0)
          StatFunc= V_maxloc
        else
          StatFunc= $xwname[x2pnt($wavenm, V_maxloc )]
        endif
```

Templates Procedures Compile

Procedure

```
    endif
    if (CmpStr(CFunc, "_Avg Int_") == 0) //average
      StatFunc= V_avg
    endif

    $outvalue[Num]=StatFunc
  endif
  Num += 1
while (gotwave)
print "x=[",hcsr(A),",",hcsr(B),"]  ( [",xcsr(A),",",xcsr(B),"] Pixel )    Recorded wave = ",outvalue," (N=",datanum-1,")"

endmacro
```

Templates Procedures

7.4. References

1. A. F. Garcia, Nonlinear Pulse Propagation in Optical Fibers, Master thesis, 2012,
2. Norwegian University of Science and Technology.
3. N. Kida, M. Hangyo, M. Tonouchi, Phys. Rev. B **62** (2000) R11965
4. F. Wooten (Editor), Optical Properties of Solids, 1972, Academic Express.
5. M. Dressel, G. Grüner (Editors), Electrodynamics of Solids: Optical Properties of Electrons in Matter, 2002, Cambridge University Press
6. V. M. Agranovich, A. A. Maradudin (Editors), Hopping Conduction of Electrons in Insulators, 1991, Elsevier Science Publishers B. V.; (B. Gudden, W. Schottky, Z. Tech. Phys. **16** (1935) 323
7. L. G. Austin, N. F. Mott, Adv. Phys. **18** (1969) 41
8. A. K. Jonscher, Nature **267** (1977) 673
9. N. A. Hegab, H. M. El-Mallah, ACTA Physica Polonica A **116** (2009) 1048

List of Publications

[1] Scientific journal

[1-1]* "Colossal magnetoresistive (La,Pr,Ca)MnO_3 nanobox array structures constructed by the three-dimensional nanotemplate pulsed laser deposition technique"
T. V. A. Nguyen, A. N. Hattori, Y. Fujiwara, S. Ueda, H. Tanaka
Applied Physics Letters, **103** (2013) 223105

[1-2]* "Estimation of dc transport dynamics in strongly correlated (La,Pr,Ca)MnO_3 film using an insulator-metal composite model for THz conductivity"
T. V. A. Nguyen, A. N. Hattori, M. Nagai, T. Nakamura, K. Fujiwara, M. Ashida, H. Tanaka
Applied Physics Letters, **105** (2014) 023502

[1-3]* "Electrical transport properties in phase-separated (La,Pr,Ca)MnO_3 nanowires investigated using terahertz time domain spectroscopy"
T. V. A. Nguyen, A. N. Hattori, M. Nagai, T. Nakamura, K. Fujiwara, M. Ashida, H. Tanaka
In preparation

[1-4] "Discrimination between gate-induced electrostatic and electrochemical characteristics in insulator-to-metal transition manganite thin films"
T. Nakamura, A. N. Hattori, **T. V. A. Nguyen**, K. Fujiwara, H. Tanaka
Applied Physics Express **8** (2015) 073201

[1-5] "Identification of Giant Mott Phase Transition of Single Electric Nanodomain in Manganite nanowall wire"
A. N. Hattori, Y. Fujiwara, K. Fujiwara, **T. V. A. Nguyen**, T. Nakamura, M. Ichimiya, M. Ashida, H. Tanaka
Nano letters, **15** (2015) 4322

Related paper

[A-1] "Effects of Mn, Cu doping concentration to the properties of magnetite nanoparticles and arsenic adsorption capacity in wastewater"
M. T. Tran, T. H. T. Nguyen, **T. V. A. Nguyen**
Applied Surface Science, **340** (2015) 166

[2] International Conference

[2-1] "Fabrication of the (La,Pr,Ca)MnO_3 nanobox structures by 3D nanotemplate PLD technique and investigation of their electronic structure"
T. V. A. Nguyen, A. N. Hattori, Y. Fujiwara, S. Ueda, H. Tanaka
The 8th Handai Nanoscience and Nanotechnology International symposium,

Osaka, Japan (Dec. 2012) （Poster）

[2-2] "Electronic structure of the (La,Pr,Ca)MnO_3 nanobox structures fabricated by 3D nanotemplate PLD technique"
T. V. A. Nguyen, A. N. Hattori, Y. Fujiwara, S. Ueda, H. Tanaka
The 13th Japan-Korea-Taiwan symposium, Osaka, Japan (Dec. 2012) （Poster）

[2-3] "Strongly correlated (La,Pr,Ca)MnO_3 nanobox array structures constructed by three dimesional nanotemplate pulsed laser deposition technique and their conductive property"
T. V. A. Nguyen, A. N. Hattori, Y. Fujiwara, S. Ueda, H. Tanaka
The 6th Vietnamese-Japanese Students' Scientific Exchange, Osaka, Japan (Sep. 2013) （Oral）

[2-4] "Investigation of effective carrier characteristics in strongly correlated (La,Pr,Ca)MnO_3 films by the THz Time Domain Spectroscopy"
T. V. A. Nguyen, A. N. Hattori, M. Nagai, T. Nakamura, K. Fujiwara, M. Ashida, H. Tanaka
The 12th SANKEN Nanotechnology Symposium, Osaka, Japan (Feb. 2014) （Poster）

[2-5] "Conductive properties through the metal insulator transition in the strongly correlated (La,Pr,Ca)MnO_3 film investigated by the THz Time Domain Spectroscopy"
T. V. A. Nguyen, A. N. Hattori, M. Nagai, T. Nakamura, K. Fujiwara, M. Ashida, H. Tanaka
The 4th International Symposium on Terahertz Nanoscience, Osaka, Japan (Mar. 2014) （Oral）

[2-6] "Estimation of dc transport dynamics using an insulator-metal composite model for THz conductivity in strongly correlated (La,Pr,Ca)MnO_3 film"
T. V. A. Nguyen, A. N. Hattori, M. Nagai, T. Nakamura, K. Fujiwara, M. Ashida, H. Tanaka
Materials Research Society 2014 Fall Meeting and Exhibit, Boston, USA (Dec. 2014) （Poster）

[2-7] "Investigation of dc transport dynamics in strongly correlated (La,Pr,Ca)MnO_3 film using an insulator-metal composite model for THz conductivity"
T. V. A. Nguyen, A. N. Hattori, M. Nagai, T. Nakamura, K. Fujiwara, M. Ashida, H. Tanaka
The 18th SANKEN International Symposium, Osaka, Japan (Dec. 2014) （Poster）

[3] Domestic conferences（Oral）

[3-1] "Investigation of effective carrier characteristics in strongly correlated (La,Pr,Ca)MnO_3 films by the THz Time Domain Spectroscopy"
T. V. A. Nguyen, A. N. Hattori, M. Nagai, T. Nakamura, K. Fujiwara, M. Ashida, H. Tanaka

The 61st JSAP Spring Meeting, (Mar. 2014)

[3-2] " Conductive properties through the metal insulator transition in the strongly correlated (La,Pr,Ca)MnO_3 film investigated by the THz Time Domain Spectroscopy"

T. V. A. Nguyen, A. N. Hattori, M. Nagai, T. Nakamura, K. Fujiwara, M. Ashida, H. Tanaka

JPS 2014 Annual (69th) Meeting, (Mar. 2014)

[4] Awards

[4-1] "**Best Student Poster Award**" in *The 18th SANKEN International Symposium*, held in Osaka, Japan, Dec. 2014

Title: "Investigation of dc transport dynamics in strongly correlated (La,Pr,Ca)MnO_3 film using an insulator-metal composite model for THz conductivity"

T. V. A. Nguyen, A. N. Hattori, M. Nagai, T. Nakamura, K. Fujiwara, M. Ashida, H. Tanaka

[4-2] "**Best Presentation Award**" in *The 4th International Symposium on Terahertz Nanoscience*, held in Osaka, Japan, Mar. 2014

Title: "Conductive properties through the metal insulator transition in the strongly correlated (La,Pr,Ca)MnO_3 film investigated by the THz Time Domain Spectroscopy"

T. V. A. Nguyen, A. N. Hattori, M. Nagai, T. Nakamura, K. Fujiwara, M. Ashida, H. Tanaka

Acknowledgements

I would like to express my sincerely gratitude to Professor Hidekazu Tanaka of Institute of Scientific and Industrial Research - Sanken, Osaka University for his advices, encouragement and stimulating discussions. Thanks to his graduation, I matured visibly in scientific research.

No word can fully express my deeply thanks Dr. Azusa N. Hattori for her continuous supports, valuable advices, and kind stimulus not only in study, but also in my daily life which have definitely strengthened me to overcome all the challenges.

I would like to thank Professor Masaaki Ashida and Associate Professor Masaya Nagai, Dr. Shigenori Ueda for their helpful advices, supports, and vital discussions.

I am deeply grateful to Associate Professor Teruo Kanki, Dr. Kohei Fujiwara and Dr. Osamu Nakagawara for their helpful advices and supports.

I would like to thank all members in Tanaka lab.: Dr. K Okada, Dr. H. Takami, Dr. Alexis S. Borowiak, Ms. W. Tingting, Mr. Y. Fujiwara, Mr. T. Kushizaki, Mr. A. Ono, Mr. T. Sakamoto, Mr. K. Kawatani, Mr. T. Ichimura, Mr. H. Ueda, Mr. S. Yamasaki, Mr. S. Sasaki, Mr. T. Hori, Mr. K. Sakai, Mr. T. Nakamura, Ms. Y. Oe, Mr. S. Tsubota, Mr. H. Nakazawa, Mr. M. Y. Li, Mr. M. Chikanari, Mr. Hayashi, and Mr. Higuchi for their support and encouragement in my laboratory life and study. I would like to thank Ms. T. Okumoto for her helpful assistance in the office procedure and encouragement in my research. The experimental assistance of Dr. S. Sakakihara, Ms. M. Sakuma, Ms. A. Iwaki, and Ms. R. Yamakage, staff of Beamline 15, SPring-8 of National Institute for Materials Science, Nanotechnology Open Facilities, Comprehensive Analysis Center, and Center of Innovation of Osaka University are gratefully acknowledged.

Last but not least, I would like to express the sincere thanks to my family and friends for their support and uninterrupted encouragement. I have received a great power with the promotion from my husband, my parents and especially, from the smiles of my lovely children.